minerals

MDPI

Article

Petrogenesis of the Newly Discovered Early Cretaceous Peralkaline Granitic Dikes in Baerzhe Area of Jarud Banner, Inner Mongolia: Implications for Deciphering Magma Evolution

Li Tian [1], Deyou Sun [1,2,*], Jun Gou [1,3], Shan Jiang [4], Zhao Feng [1], Duo Zhang [1] and Yujie Hao [5]

[1] College of Earth Sciences, Jilin University, Changchun 130061, China
[2] State Key Laboratory of Ore Deposit Geochemistry, Institute of Geochemistry, Chinese Academy of Sciences, Guiyang 550081, China
[3] Fundamental Science on Radioactive Geology and Exploration Technology Laboratory, East China University of Technology, Nanchang 330013, China
[4] The No. 243 Team of Nuclear Industry, Chifeng 024000, China
[5] Key Laboratory of Mineral Resources Evaluation in Northeast Asia, Ministry of Natural Resources, Changchun 130061, China
* Correspondence: sundy@jlu.edu.cn; Tel.: +86-135-0080-7923

Abstract: The super-large Baerzhe Be–Nb–Zr–REE deposit in NE China is hosted in the Early Cretaceous peralkaline granites. In this work, the newly discovered granitic dikes developed around the Baerzhe deposit were studied for the first time, focusing on their genesis and genetic relationships with the Baerzhe peralkaline granites. Zircon U-Pb dating of these granitic rocks (including the granite porphyry, rhyolite and miarolitic granite) yielded Early Cretaceous ages of 125–121 Ma. Their mineral assemblages and geochemical features suggest that they share similar features with the peralkaline A-type granites. Their geochemical data and zircon Hf isotopic compositions ($\varepsilon_{Hf}(t)$ = +3.4 to +10.5) indicate that the peralkaline granitic rocks were formed by the partial melting of dehydrated charnockite with extensive plagioclase crystal fractionation, which resulted in a peralkaline affinity. There are two types of distinct zircons in the studied samples: the type I zircon with a bright rim and dark core, which may represent a cumulate mineral phase captured together with aggregates during eruption, and the type II zircon with a higher evolution degree crystallized in the residual melts. Combined with the simulation results using whole-rock trace elements, we proposed that the peralkaline granitic dikes represent more evolved interstitial melts than the Baerzhe granitic magma. In the Early Cretaceous extensional tectonic settings, mantle-derived magma upwelled, which induced the melting of the lower crust and prolonged the evolutionary process of the magma crystal mush.

Keywords: Baerzhe; peralkaline granitic dikes; petrogenesis; crystal mush model

Citation: Tian, L.; Sun, D.; Gou, J.; Jiang, S.; Feng, Z.; Zhang, D.; Hao, Y. Petrogenesis of the Newly Discovered Early Cretaceous Peralkaline Granitic Dikes in Baerzhe Area of Jarud Banner, Inner Mongolia: Implications for Deciphering Magma Evolution. *Minerals* **2022**, *12*, 1532. https://doi.org/10.3390/min12121532

Academic Editor: Frederick Lin Sutherland

Received: 29 October 2022
Accepted: 25 November 2022
Published: 29 November 2022

1. Introduction

The possible genetic relationships between the concomitant plutonism and volcanism, as well as their evolution processes, are controversial [1–6]. Some field and geochronologic studies have suggested that volcanic rocks grow rapidly and erupt almost completely, whereas pluton growth usually takes a long time, possibly millions of years [1,3,6], indicating that evolutionary processes between volcanism and plutonism are different. However, in some cases, the coexisting volcanic rocks and plutons with similar isotope compositions were thought to have derived from the same magma chamber and interpreted as a mush model [7–9]: the volcanic rocks (most of them are usually felsic with high SiO_2 content) are produced by the interstitial melt extracted from the long-lived and shallow-crustal crystal mush or formed by thermal rejuvenation of near-solidus granitic mushes, and the crystalline residues solidify as plutons [4,5,10–12]. However, a problem remains: the dynamic mechanisms of interstitial melts' extraction and eruption are poorly constrained, and the magma chamber lifespans are also controversial [11–16]. Moreover, if the highly

evolved felsic volcanic rocks represent the interstitial melts, they must be accompanied by a reservoir of cumulates with complementary geochemical features [17]. However, the felsic volcanic rocks coexisting with the granites also show high-silica and highly evolved features [18,19]. Are the concomitant felsic plutons rocks residual cumulates or "frozen" melts? More and further studies are needed to understand the genetic relationships between the associated felsic volcanic rocks and plutons.

The Baerzhe deposit in NE China is a super-large REE-Nb-Be-Zr deposit, which was hosted in the peralkaline granites (which we call Baerzhe granites in this study). Predecessors have carried out a lot of research on this deposit, mainly focusing on the petrogenesis and mineralization of the ore-forming granites [20–26], but debate remains. Some studies suggested that the Baerzhe granites were formed by the melting of a juvenile mantle component [20,24]; while the oxygen isotope composition of magmatic zircons selected from Baerzhe granites with slightly lower $\delta^{18}O$ value than that of the mantle suggested that the Baerzhe granites may be formed by the partial melting of oceanic crust that underwent hydrothermal alteration [27–29]. In addition, mineralization and alteration may alter the rock composition, making it unable to reflect the characteristics of the original magma.

Recently, we found a large number of peralkaline granitic dikes occurring around the Baerzhe deposit. Magmatic rocks from these dikes have similar mineral assemblages with the Baerzhe granites. Both of these dikes and Baerzhe granites intruded into the Baiyingaolao Formation with no cutting-through relationship between them. Their close spatial and temporal relationships imply a potential genetic connection between them, which therefore provides an opportunity to use the mush model to explain the subvolcanic–plutonic genesis connections.

In this study, we conducted petrographical, whole-rock and mineral geochemical, and zircon U-Pb and Hf isotopic analyses for the peralkaline granitic dikes from the Baerzhe area, with the aims to (1) constrain the magma source, (2) clarify the genetic relationships between the peralkaline granitic dikes and Baerzhe granites, and (3) reveal the formation mechanisms of the highly evolved peralkaline magmas.

2. Geology and Petrography

2.1. Regional Geology

The Xingmeng (Xing'an–Mongolian) orogenic belt represents the eastern part of the Central Asian Orogenic Belt, and consists of the Erguna, Xing'an, Songliao, and Jiamusi blocks from west to east. These microcontinental blocks were amalgamated during the Paleozoic [29–31]. The study area was located in the south of the Xing'an block, adjacent to NE-trending Xilinhot–Heihe suture zone (Figure 1a). Voluminous Jurassic to Cretaceous igneous were developed in this area in an extensional back-arc environment, which is related to the westward subduction of the Paleo-Pacific plate and the closure of the Mongol–Okhotsk Ocean [32–34].

The Baerzhe deposit was hosted by the Early Cretaceous Baiyingaolao Formation and the Manitu Formation (Figure 1b). The Baiyingaolao Formation was formed at 141–124 Ma, with a peak age of 130 Ma. It consists mainly of rhyolite, rhyolitic tuff, and ignimbrite. The Manitu Formation is mainly composed of intermediate volcanic rocks and pyroclastic rocks, including andesite and andesitic breccia tuff, which were mainly formed between 131 and 152 Ma [35,36]. Numerous dikes and stocks occurred in the study area, such as granite porphyry, quartz porphyry, monzoporphyry, diorite porphyrite, and rhyolite porphyry. These dikes intruded into the Baiyingaolao and Manitu formations in NNE-trending and nearly NS-trending, indicating that they were mainly formed during the Early Cretaceous.

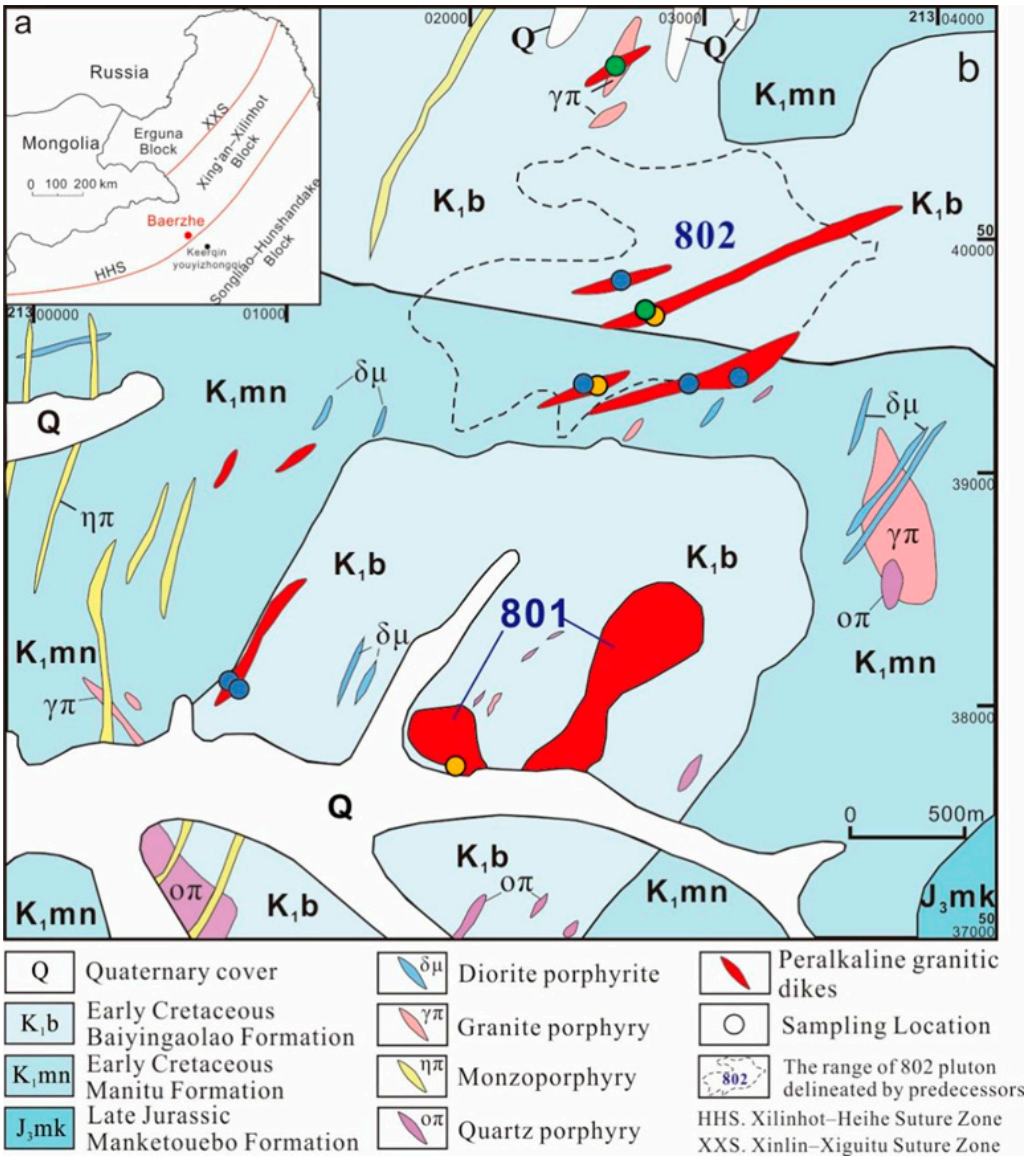

Figure 1. (**a**) Tectonic sketch map of NE China; (**b**) Geological map of Baerzhe ore district and its vicinity; modified after Yang, Niu [27] and reference therein; the blue filled circle is the peralkaline rhyolite sampling location; the green one is peralkaline granite porphyry and the yellow one is the peralkaline miarolitic granite; 801 in the figure represents the Baerzhe granite, which is also the Baerzhe deposit.

The peralkaline granites at Baerzhe are divided into the east body (ca. 0.24 km^2) and the west body (ca. 0.11 km^2) at the surface (Figure 1a). The west body is characterized by miarolitic texture with weak mineralization, whereas the east body with strong albitization and silicification is the main ore-bearing body in the Baerzhe deposit. The east body is composed mainly of a strongly mineralized granite (which we call Baerzhe mineralized granites in this study) in the upper part, and a barren granite (which we call Baerzhe barren granites in this study) in the lower part [21,24]. The Baerzhe mineralized granites mainly consist of K-feldspar, quartz, sodic-amphiboles, and albites, characterized by the extensive development of sodium alteration; the mineralization intensity is positively correlated with the degree of albitization [37]. The Baerzhe barren granites have similar mineral assemblages with Baerzhe mineralized granites except for albites. Moreover, barren granite occurred at the top of the pluton, with unidirectional solidification textures, which is usually

evidence of saturated volatiles in magma [38]. The Baerzhe mineralized granites have been previously dated, yielding the relatively consistent results of 123–127 Ma [21,23,39].

About 1.5–2 km north of the Baerzhe granites, a larger peralkaline granitic pluton (also referred to as 802 granitic pluton; [26]) with an exposed area of 1.25 km^2 was exposed (Figure 1b). Previous studies show that the 802 granitic pluton is barren; although, it shares similar geochemical characteristics and a magma source with the Baerzhe granites [26]. According to our field investigation, the 802 granitic pluton is mainly composed of felsic volcanic and subvolcanic rocks such as rhyolites, rhyolitic crystal fragment tuff, rhyolite porphyries, and granite porphyries, and a series of peralkaline granitic dikes. The peralkaline granitic dikes are generally NE-NNE trending with variable scales ranging from several to hundreds of meters in length Figure 1b. Compared with the Baerzhe granites, the occurred altitude of these peralkaline granitic dikes is generally higher, ranging between 950 and 1073 m.

2.2. Petrography

Based on the petrographic characteristics, we divided the investigated peralkaline granitic rocks in the Baerzhe area into three types: peralkaline granite porphyry, peralkaline rhyolite, and peralkaline miarolitic granite.

The peralkaline rhyolite can be divided into two types and both of them are crystal-poor rhyolites. One of them exhibits porphyritic texture and flow structure (Figure 2a,b,d,e). Their phenocrysts comprise about 5%–10% of the rock by volume and are mainly composed of quartz and alkali feldspar. The groundmass consists of sodic amphibole, quartz, and K-feldspar (Figure 2d). The other type of the peralkaline rhyolite develops a spherulite structure (Figure 2c,f). The spherulites are mainly composed of radial sodic amphibole and K-feldspar, with a content of about 35%–40%. The groundmass consists of minor felsic particles and acicular sodic amphibole.

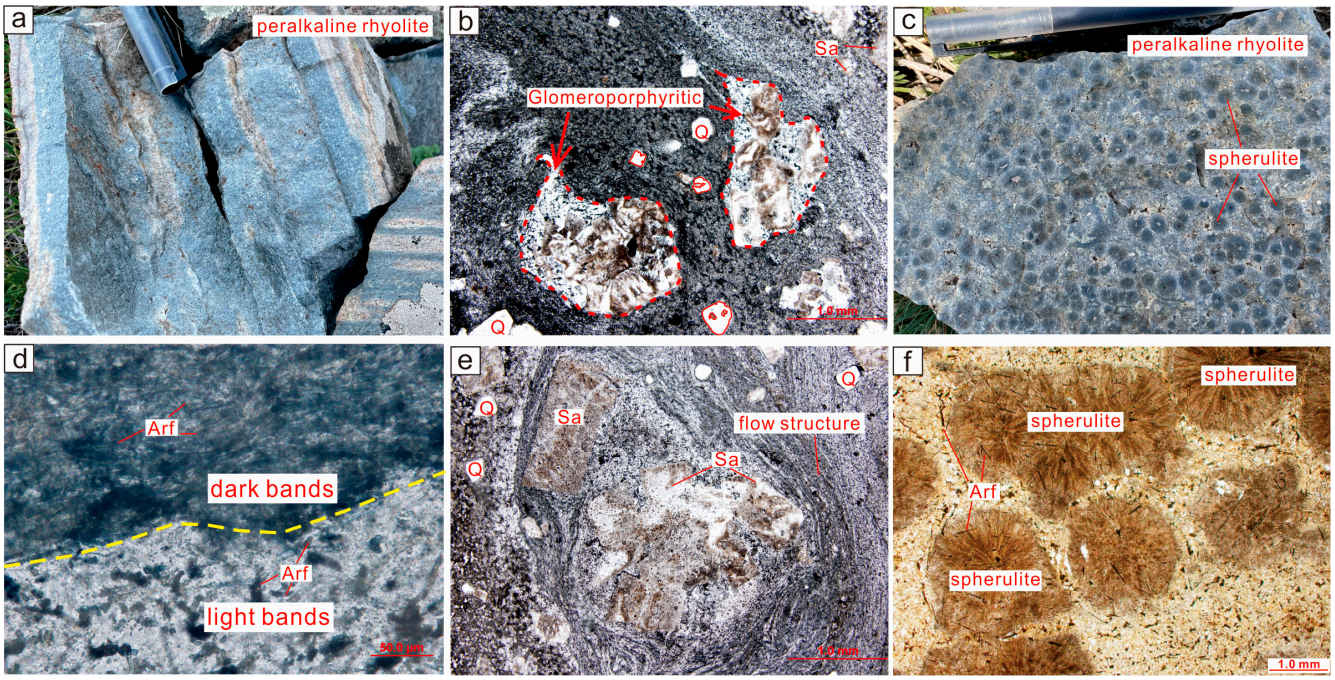

Figure 2. Photographs and photomicrographs of the peralkaline rhyolite dikes in the Baerzhe area. (**a**) Peralkaline rhyolite with flow structure; (**b**) Glomeroporphyritic in peralkaline rhyolite; (**c**) Peralkaline rhyolite with spherulite structure; (**d**) Different bands in the peralkaline rhyolite with flow structure; (**e**) Phenocrysts in the peralkaline rhyolite; (**f**) Photomicrographs of the spherulite in peralkaline rhyolite. Abbreviations: Q = Quartz; Arf = Arfvedsonite; Sa = Sanidine.

The peralkaline granite porphyry comprises phenocrysts of K-feldspar and quartz (vol. 20%–25%; Figure 3a,b). The glomeroporphyritic aggregates have a similar mineral composition to that of peralkaline rhyolite (Figure 3c). The groundmass exhibits fine- to micro-grained textures and consists of sodic amphibole, K-feldspar, and quartz.

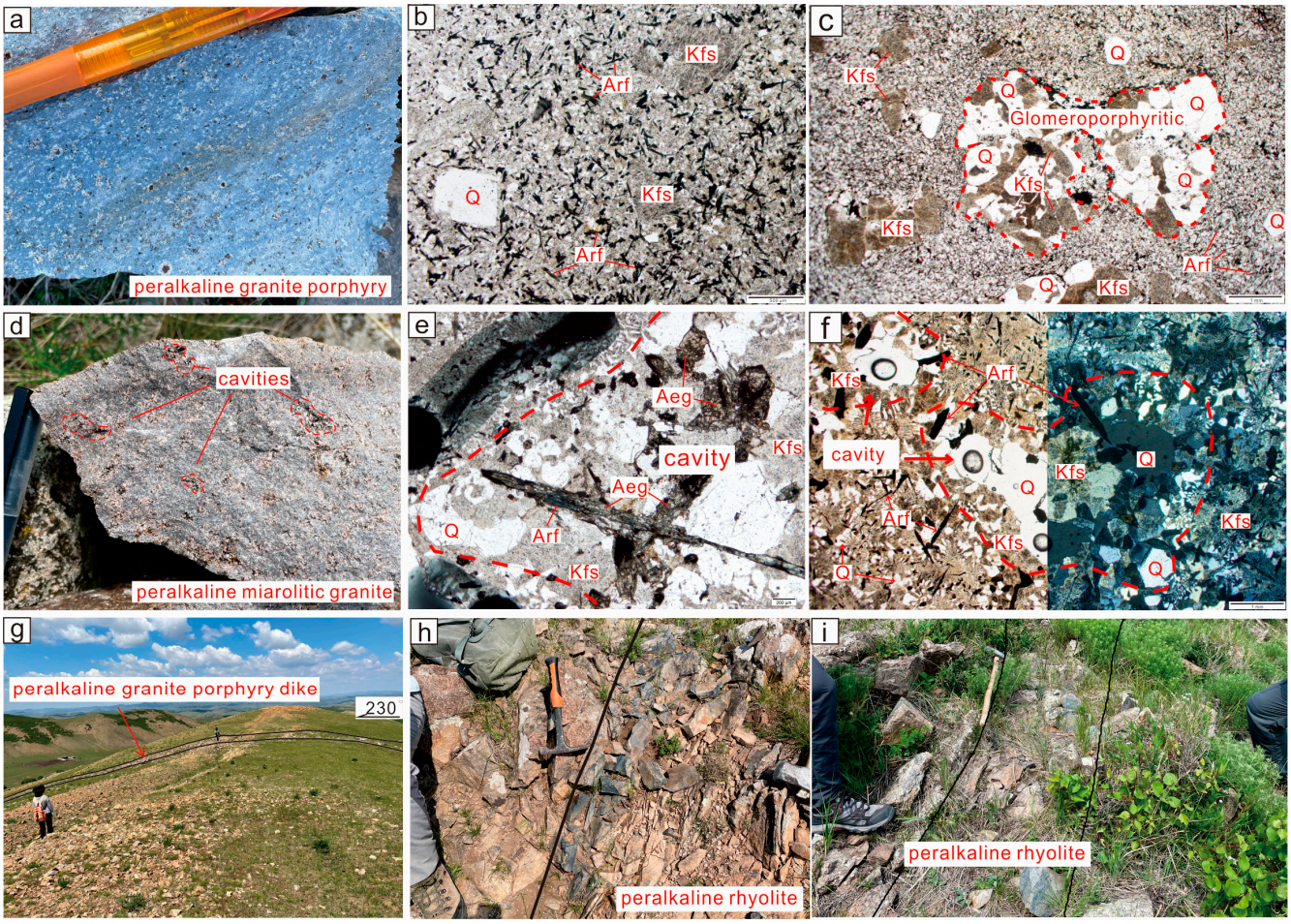

Figure 3. Photographs and photomicrographs of the peralkaline granite porphyry and peralkaline miarolitic granite dikes in the Baerzhe area. (**a**) Photograph of hand specimen of the peralkaline granite porphyry; (**b**) Photomicrograph of peralkaline granite porphyry; (**c**) Glomeroporphyritic in peralkaline granite porphyry; (**d**) Cativities in peralkaline miarolitic granite; (**e**) The arfvedsonite in cativities of peralkaline miarolitic granite were altered to aegirine; (**f**) Photomicrograph of cativities in peralkaline miarolitic granite; (**g**) The field photograph of peralkaline granite porphyry dike; and (**h**,**i**) Contact relationship between the peralkaline rhyolite and the surrounding rocks (The black solid line is the boundary line of the dike). Abbreviations: Q = Quartz; Arf = Arfvedsonite; Kfs = K-feldspar; Aeg = Aegirine.

The cavities of the peralkaline miarolitic granite are usually filled with granular quartz, K-feldspar, and sodic amphibole (Figure 3d–f). Sodium alteration occurs in some samples, which shows that the sodic amphiboles in both the cavities and the groundmass were partially altered to aegirine (Figure 3e). This type of rock is mainly composed of fine-grained K-feldspar, quartz, and euhedral acicular sodic amphibole, with a grain size of 0.5–1.0 mm. The intergrowth of quartz and K-feldspar constitutes a micrographic texture (Figure 3f).

The sodic amphiboles in the samples are typically magmatic. Most of them are euhedral–subhedral acicular or acicular columnar in shape and coexist with felsic minerals (Figure 3b,c,f). Only in one of the peralkaline miarolitic granite samples were the sodic

amphiboles partially altered to aegirine (Figure 3e), which may be related to the sodic alteration [21]. In all types of rock, the accessory minerals are mainly composed of zircon and Fe-Ti oxide; the peralkaline miarolitic granite contains a small amount of rare earth carbonate minerals (Figure 4a,c). The zircon in all types of rock is mainly filled in the interstices of the main rock minerals, indicating that it crystallized late (Figure 4b).

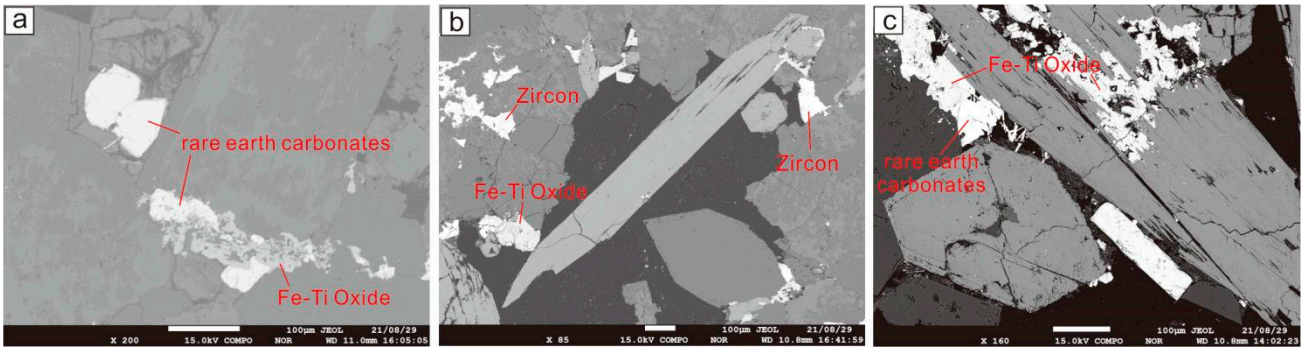

Figure 4. BSE of the accessory minerals in peralkaline miarolitic granite. (**a**) The rare earth carbonates and Fe-Ti Oxide in peralkaline microlitic granite; (**b**) Interstitial zircons in peralkaline microlitic granite; (**c**) the rare earth carbonates and Fe-Ti Oxide in peralkaline microlitic granite.

3. Analytical Methods

3.1. Whole-Rock Major and Trace Elements

Whole-rock major and trace element contents for 18 peralkaline granitic samples in this study were analyzed at the Key Laboratory of Mineral Resources Evaluation in Northeast Asia, Ministry of Natural Resources, China; the data are listed in Supplementary Table S1. All fresh samples were powdered in an agate ring mill to less than 200 mesh. X-ray fluorescence (XRF) and ICP–MS (Agilent 7500a) were used to measure the major and trace elements compositions, respectively. The national standard sample 07103 (granite) and sample 07105 (basalt) were used as standard samples to monitor the accuracy and error of analysis. The method for X-ray fluorescence analysis of major elements was established by pressing the powder into disks directly, with analytical errors within 5% [40]. As for trace element analysis, about 60 mg of sample powder was digested by HF + HNO_3 in Teflon bombs, then they were analyzed in an Agilent 7500a ICP-MS [41]. When the content of trace elements exceeds 10 μg/g, the relative deviation is less than 5%; otherwise, the relative deviation is less than 10%.

3.2. Zircon U-Pb Dating, Trace Elements, and Hf Isotope Analyses

The zircons were separated at the Langfang Geological Service Co. Ltd., Langfang, China. The age and trace elements of all zircons were measured using laser ablation-inductively coupled plasma-mass spectrometry (LA-ICP-MS) at the Key Laboratory of Mineral Resources Evaluation in Northeast Asia, Ministry of Natural Resources of China, China. Laser sampling was conducted using a GeoLas 200 M 193 nm ArF excimer laser ablation system, and its spot diameter is 32 μm. The detailed analytical procedures were given in Liu, Gao [42]. Standard zircon 91,500 [43] was analyzed every other five-spot analysis for external correction of isotope ratio, NIST SRM 610, and Plešovice [44] were analyzed every other ten-spot analysis as the external standard and the monitoring blind sample, respectively. Isotope ratios were calculated via the Glitter software (Macquarie University, Sydney, Australia), and common Pb was corrected based on the method proposed by Andersen [45]. The Isoplot v. 3.0 software [46] was used to calculate the weighted mean average age.

Zircon Hf isotopes were analyzed using a GeoLas Pro UP193nm laser-ablation microprobe, attached to a Neptune multi-collector ICP-MS in the MNR Key Laboratory of Metallogeny and Mineral Assessment, Institute of Mineral Resources, Chinese Academy

of Geological Sciences (CAGS), Beijing. Detailed instrumental conditions, experimental procedures, and data acquisition were introduced in Hou, Li [47]. The analysis was performed using 44 μm diameter spot at 8 Hz and a fluence of 8–10 J/cm^2. In order to correct for the isobaric interferences of ^{176}Lu and ^{176}Yb on ^{176}Hf, ^{176}Lu/^{175}Lu = 0.02658 and ^{176}Yb/^{173}Yb = 0.796218 ratios were determined [48]. We normalized Yb isotope ratios to ^{172}Yb/^{173}Yb of 1.35274 and Hf isotope ratios to ^{179}Hf/^{177}Hf of 0.7325 by using the exponential law [48] for instrumental mass bias correction. Zircon GJ-1 was used as the reference standard, with a weighted mean ^{176}Hf/^{177}Hf ratio of 0.282018 ± 0.000020 (2σ, n = 3) during our routine analysis, which is essentially the same as the weighted mean ^{176}Hf/^{177}Hf ratio of 0.282013 ± 0.000019 (2σ) by Elhlou, Belousova [49].

One peralkaline miarolitic granite sample (20S50-6), one peralkaline granite porphyry sample (20S51-1), and three samples of peralkaline rhyolite (21S64-1/21S74-3/20S43-3) were chosen for in situ single-spot zircon U-Pb dating and Hf isotope analysis, the data are summarized in Supplementary Tables S2 and S3, respectively; the trace elements analysis data of selected zircons are given in Supplementary Table S4.

3.3. Mineral Chemistry

Mineral composition analysis of amphiboles was performed at the State Key Laboratory of Ore Deposit Geochemistry, Chinese Academy of Sciences at Guiyang with a JXA8230 microprobe. According to the size of the amphiboles, the operating conditions of the microprobe were a 1–10 μm electron beam, 25 kV of accelerating voltage, and a sample current of 10 nA. The analytical uncertainties are within 2%. The mineral formulae were calculated on the basis of O + OH + F = 24 atoms per formula unit (apfu) and OH = 2-2Ti, using the amount of Ti^{4+} as a proxy for the (maximum) oxy-component in the mineral structure [50]. The formula calculation was performed following the latest IMA 2012 recommendations [50,51] using the Excel spreadsheet of Locock [52]. We selected unaltered amphiboles in different types of rocks for major elements analyses, the analysis data of them are listed in Supplementary Table S5.

4. Results

4.1. Major- and Trace-Elements Geochemistry

All of the samples have high SiO_2 contents of 73.69 to 76.35 wt%, high total alkali content (ALK) of 6.94–8.96 wt%, low P_2O_5 (0.01–0.03 wt%), TiO_2 (0.13–0.21 wt%), MgO (0.01–0.10 wt%), and CaO (0.07–0.45 wt%) contents. All the samples show the characteristics of peralkaline (Figure 5a) and alkalic to alkali-calcite features (Figure 5b). The Fe-index versus SiO_2 diagram (Figure 5c) shows that these samples are ferroan granites. On the chondrite-normalized REE distribution diagram (Figure 5d), all of the studied samples show a light LREE enrichment, nearly flat HREE curve, and obvious negative Eu anomalies (δEu = 0.02–0.05), which are characterized by a V-shaped pattern. The contents of ∑REE range from 316 to 957 ppm with $(La/Yb)_N$ ratios of 4.26 to 11.19. On the primitive mantle normalized multi-element diagram (Figure 5e), all the samples are commonly characterized by high concentrations of high field strength elements (HFSEs) such as Th, U, and Zr but marked depletion in Cs, Ba, K, and Ti.

The diagrams of Zr/δEu versus Al_2O_3 (Figure 5f,i) show that these samples exhibit a well-defined chemical variation trend. With Al_2O_3 contents decreasing, the Zr gradually enriched from Baerzhe barren granites to the peralkaline granitic dikes; the δEu values decreased with the reduction of Al_2O_3 contents, which is consistent with the evolution trend of magma differentiation. Moreover, the contents of REE and Zr show a gradually increasing trend from Baerzhe barren granite, peralkaline granite porphyry, and peralkaline rhyolite to peralkaline miarolitic granite (Figure 5h,i). The Baerzhe barren granites with the highest Al_2O_3 contents and δEu values were formed by magma with a relatively low evolution degree; the peralkaline granitic dikes were formed by a more evolved melt.

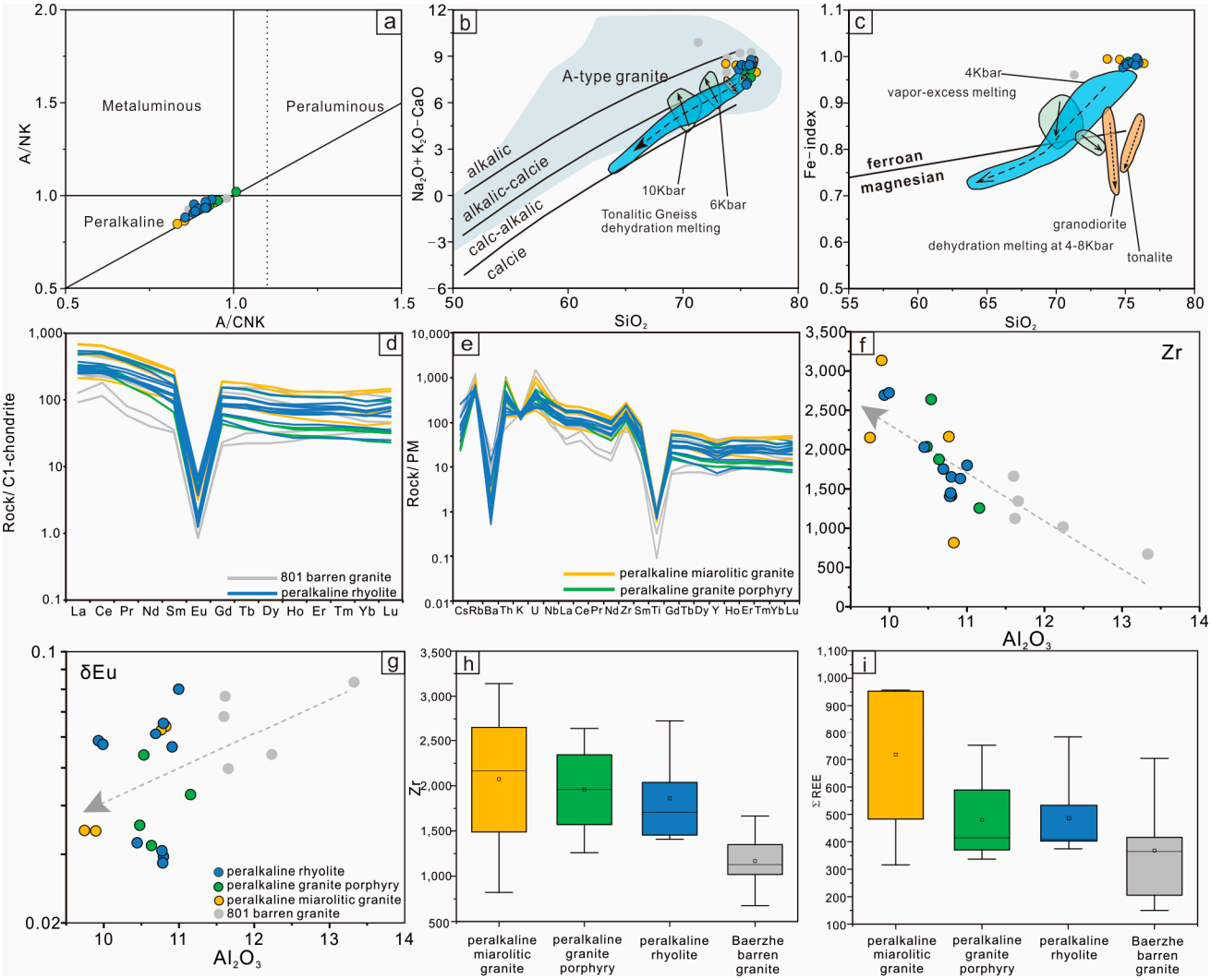

Figure 5. (**a**) A/NK (molar $Al_2O_3/(Na_2O + K_2O)$) versus A/CNK (molar $Al_2O_3/(CaO + Na_2O + K_2O)$); fields after Shand [53] for studied samples; (**b**) $Na_2O + K_2O$-CaO (wt%) versus SiO_2 (wt%); fields after Frost and Frost [54]; (**c**) Fe-index ($(FeO + 0.9Fe_2O_3)/(FeO + 0.9Fe_2O_3 + MgO)$) versus SiO_2 (wt%); fields after Frost and Frost [54]; (**d**) Chondrite-normalized REE patterns of the peralkaline granitic rocks and (**e**) Primitive mantle-normalized multi-element variation diagrams of the peralkaline granitic rocks; the normalization values for primitive mantle and chondrite are from Sun and McDonough [55]; (**f**) Zr versus Al_2O_3 and (**g**) δEu versus Al_2O_3 for the peralkaline granitic dikes and Baerzhe barren granite; Box chart of Zr (**h**) and ΣREE (**i**) of the peralkaline granitic dikes and Baerzhe barren granite (Horizontal line within the box and square represent median and mean respectively); data sources of the Baerzhe barren granite: Bor-ming Jahn [20]; Yang, Shan [26]; Su, Jiang [24], the following are the same.

4.2. Zircon U-Pb-Hf Isotopes and Trace Elements

4.2.1. Zircon U-Pb-Hf Isotope Composition

The subsets of the isotopic ages are illustrated on the Concordia diagram in Figure 6. All of the analyses of zircons from the peralkaline rhyolites (21S64-1/20S43-3/21S74-3) are concordant (Figure 6), with 9 spot analyses from sample 21S64-1 yielding a weighted mean $^{206}Pb/^{238}U$ age of 123.3 ± 3.3 Ma (MSWD = 1.8); 19 spot analyses from sample 21S74-3 yielding a weighted mean $^{206}Pb/^{238}U$ age of 122.5 ± 1.4 Ma (MSWD = 0.36); and 22 spot analyses from sample 21S74-3 yielding a weighted mean $^{206}Pb/^{238}U$ age of 121.3 ± 1.2 Ma (MSWD = 1.2). The initial $^{176}Hf/^{177}Hf$ ratios of 21S64-1 and 21S74-3 range from 0.282850

to 0.282960 and 0.282810 to 0.282910, with $\varepsilon_{Hf}(t)$ values from +5.2 to +9.0 and +3.8 to +7.2 respectively. The $\varepsilon_{Hf}(t)$ of 20S43-3 range from +7.4 to +10.5.

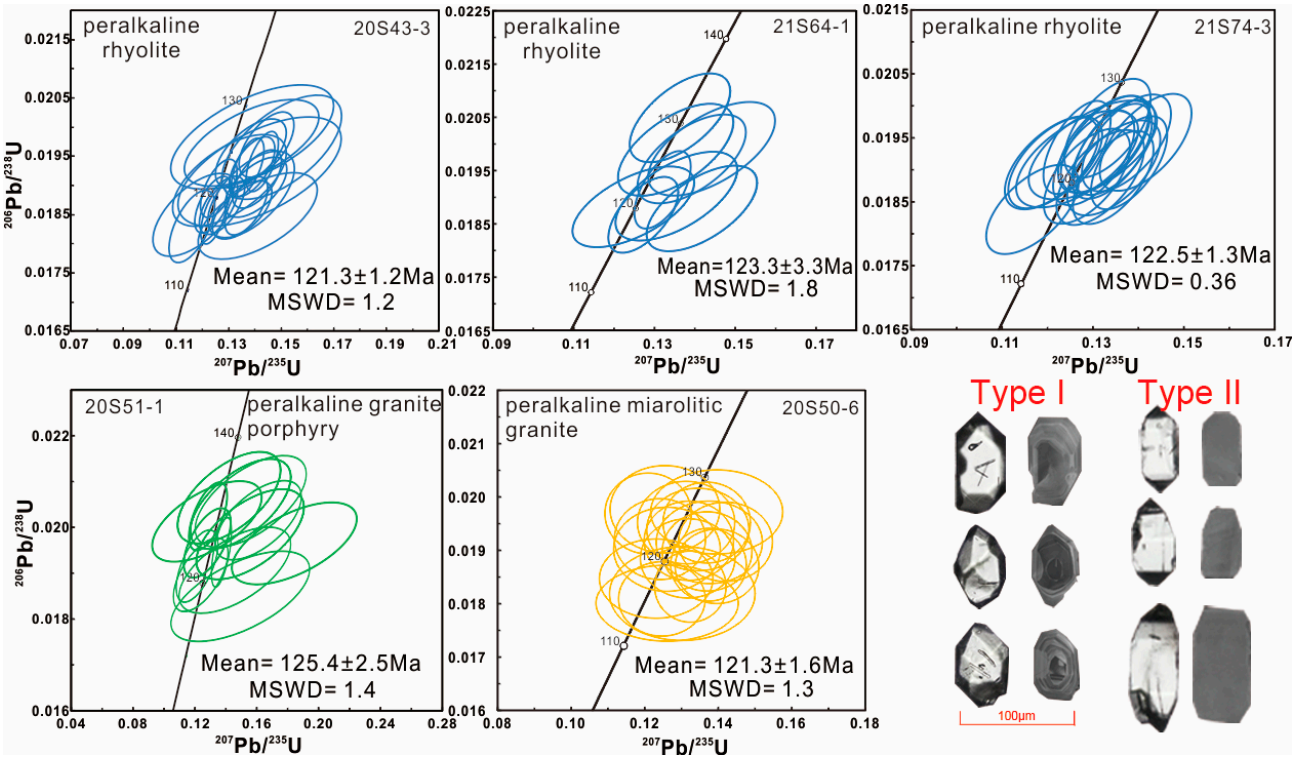

Figure 6. In situ LA-ICP-MS U-Pb Concordia diagrams of zircons from different peralkaline granitic rocks and the CL image of two types of zircons.

The $^{206}Pb/^{238}U$ ages of peralkaline granite porphyry (20S51-1) range from 118 to 132 Ma, giving a weighted-mean $^{206}Pb/^{238}U$ age of 125.4 ± 2.5 Ma (mean square of weighted deviations (MSWD) = 1.4, n = 13). The initial $^{176}Hf/^{177}Hf$ ratios of 20S51-1 range from 0.282800 to 0.282900, with corresponding $\varepsilon_{Hf}(t)$ values from +3.4 to +7.0.

The weighted mean age of the peralkaline miarolitic granite sample (20S50-6) is 121.3 ± 1.6 Ma (MSWD = 1.3, n = 20). Its initial $^{176}Hf/^{177}Hf$ ratio varies from 0.282870 to 0.282920 and the corresponding $\varepsilon_{Hf}(t)$ values range from +5.9 to +7.9. All the peralkaline granitic samples display consistent zircon U-Pb ages (Figure 6) and Hf isotopic compositions (Figure 7a).

4.2.2. Zircon Trace Elements

The zircon grains from peralkaline granite porphyry and peralkaline rhyolites can be divided into two types according to their different crystal form and internal structural domains (Figure 6). The first type (Type I) zircons range in size from 50 to 100 μm, having well-developed {101} pyramids. The CL images of zircon usually show clear oscillatory zonation and CL-bright occurring as the rim of the dark core. The second type (Type II) zircons have euhedral short-prismatic forms, ranging in size from 100 to 150 μm, with well-developed {101} pyramids and {100} prisms, which are similar to the zircon crystalized in the alkaline magma [56]. The zircon grains are dark in CL images with no obvious oscillatory zonation, and most of them contain abundant mineral inclusions.

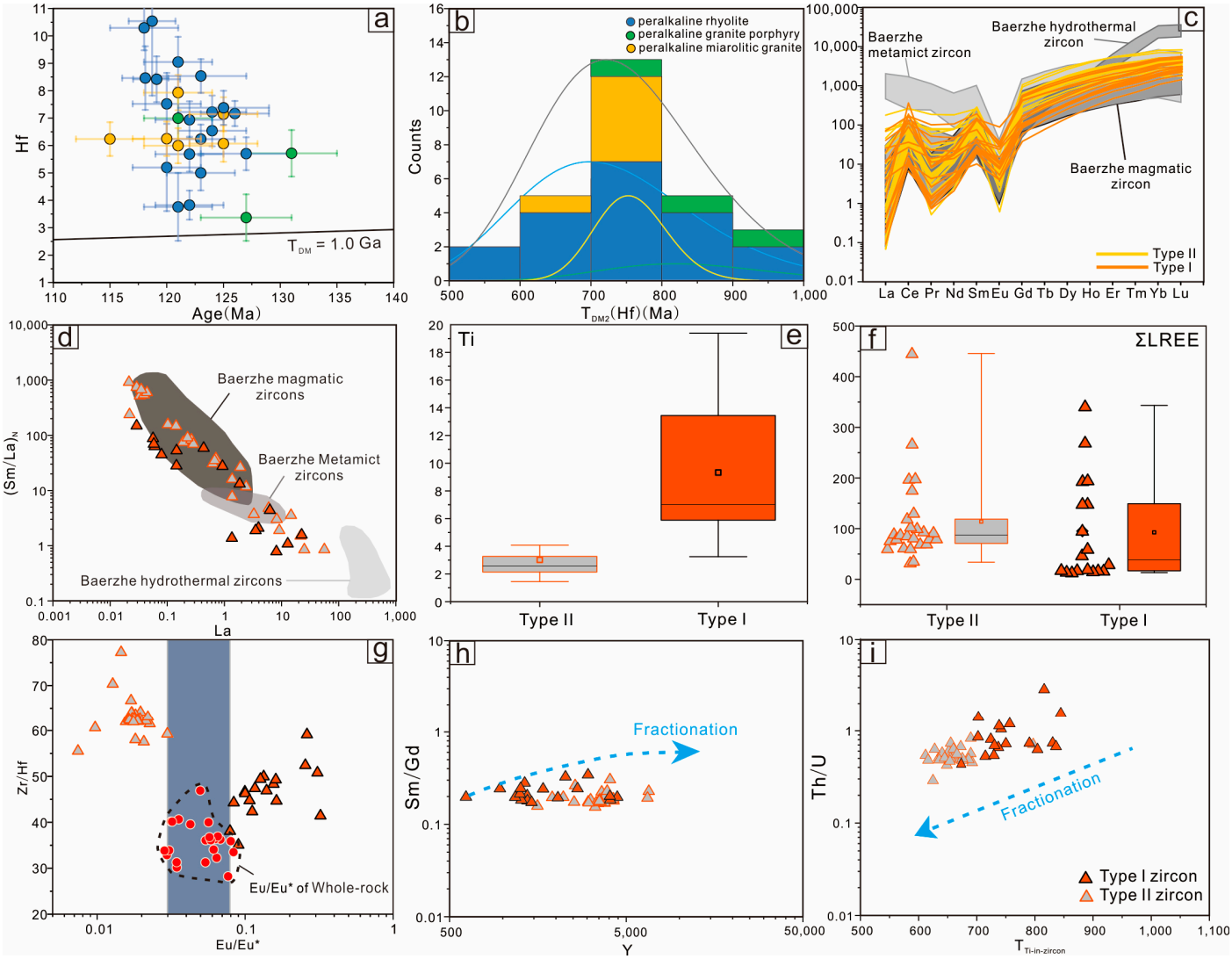

Figure 7. (**a**) Compilation of zircon $\varepsilon_{Hf(t)}$ versus age for the peralkaline granitic rocks; (**b**) T_{DM2} age data histograms of the peralkaline granitic rocks; (**c**) Chondrite-normalized REE patterns of the two types of zircon; the normalization values for chondrite are from Sun and McDonough [55]; (**d**) $(Sm/La)_N$ versus La of the two types of zircon; data source of the Baerzhe magmatic/metamict/hydrothermal zircons is from Yang, Niu [27]; (**e**,**f**) Box chart of Ti and ΣREE of the two types of zircon from peralkaline granite porphyry and peralkaline rhyolite (Horizontal line within the box, orange square and black diamond represent median, mean, and far outliners, respectively); (**g**) Zr/Hf versus Eu/Eu*; (**h**) Sm/Gd versus Y and (**i**) Th/U versus $T_{Ti\text{-}in\text{-}zircon}$ diagram of the two types of zircon.

Both Type I and Type II zircons have pronounced positive Ce anomalies and negative Eu anomalies in the REE patterns diagram, which is consistent with the Baerzhe magmatic zircons (Figure 7c). Type I zircon grains with oscillatory zonation have a total REE content of 490–3006 ppm and show enrichments in HREE (LREE/HREE = 0.02–0.21), with Ti content of 3.25–19.39 ppm; the ratio of Eu/Eu* of type I is 0.08–0.32 and the Th/U ratios is 0.43–2.80. Type II zircon grains have higher total REE concentrations ranging from 1030 to 4984 ppm and lower Eu/Eu* ratios of 0.01–0.02 compared with Type I. Type II zircon also show enrichments in HREE (LREE/HREE = 0.02–0.16), with low Ti content of 1.45–12.51 ppm and Th/U ratios of 0.29 to 0.82. Based on the morphology and Th/U ratios, all the studied zircons are consistent with the characteristics of the magmatic zircon. In the $(Sm/La)_N$ versus La diagram (Figure 7d), some data points are plotted in the transition

area between magmatic zircon and hydrothermal zircon. The development of inclusions in the studied zircons would be the cause of La concentrations and $(Sm/La)_N$ ratios reduction, resulting in magmatic zircon that shows the "characteristics" of hydrothermal zircon [57].

Zircon Ti temperatures were calculated based on the equation proposed by Kirkland, Smithies [58]. All samples have high SiO_2 contents and are quartz-bearing, indicating that silica was saturated during the zircons' crystallization. Therefore, we assumed the $a_{SiO_2} = 1$. The a_{TiO_2} of most granitic rocks varies between 0.6 and 0.9 [59]. No rutile was found in the studied samples, and the Ilmenite was mainly of late-altered minerals rather than magmatic crystallization [22], indicating that the Ti is undersaturated. We assumed $a_{TiO_2} = 0.75$ for calculation. In the same magmatic system, a_{TiO_2} is constant with zircon crystalizing. We only use the zircon Ti temperatures to reflect the magma evolution process with decreasing temperature, so, a loosely constrained a_{TiO_2} should be workable. The results of Type I zircon crystallized between 673 and 844 °C, with an average temperature of 756 °C; and the Type II crystallized between 612 and 796 °C, with an average of 660 °C, lower than Type I.

4.3. Mineral Chemistry of Amphibole

The chemical compositions, site assignments, and species names of amphiboles are listed in Supplementary Table S5. Almost all of them in this study are of the sodic subgroup (riebeckite or arfvedsonite). The type of amphibole in peralkaline miarolitic granite is mainly arfvedsonite ($^A(Na + K) \geq 0.5$), while the type of amphibole in peralkaline rhyolite is riebeckite ($^A(Na + K) < 0.5$) [60].

Typical core-rim compositional profiles are presented in Figure 8. They show a relatively consistent element variation. From core to rim, F, Na^+ and $(Na + K)/Al$ ratios increase with Ca^{2+} and Al contents decreasing. The Fe^{3+} content gradually increases at first, and then decreases sharply at the rim. The variation in Fe^{2+} is actually the opposite. Because of the lack of calcic compositions, the sodic amphiboles show relatively short and evolved compositional trends in the $Ca + Al^{IV}$ versus $Si + Na + K$ diagram (Figure 9; Strong and Taylor [61]). They crystalized under progressively (alkali, Si)-rich and Ca-poor conditions, which is consistent with the magmatic trends. Compared with the sodic amphiboles in peralkaline rhyolite, the composition of sodic amphiboles in the groundmass of peralkaline miarolitic granite has more evolved features with relatively low CaO and high alkali contents (Figure 9).

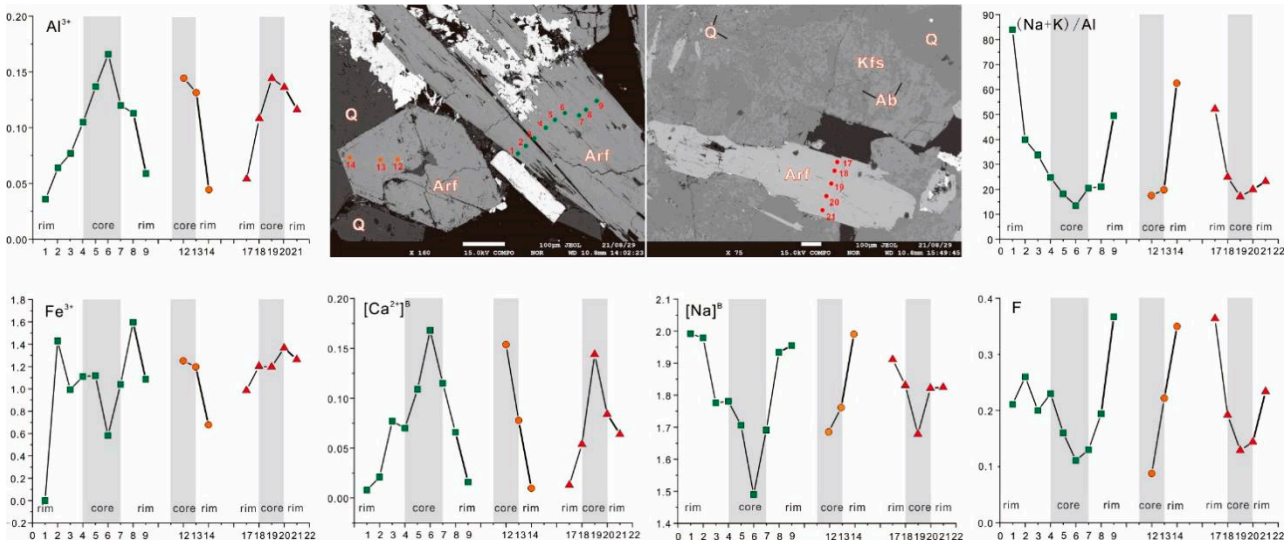

Figure 8. Rim–core cationic (apfu) profiles describing the main compositional variations in selected arfvedsonite of peralkaline miarolitic granite. The color in the rim–core cationic (apfu) profiles is consistent with that in BSE. Q = Quartz; Arf = Arfvedsonite; Kfs = K-feldspar.

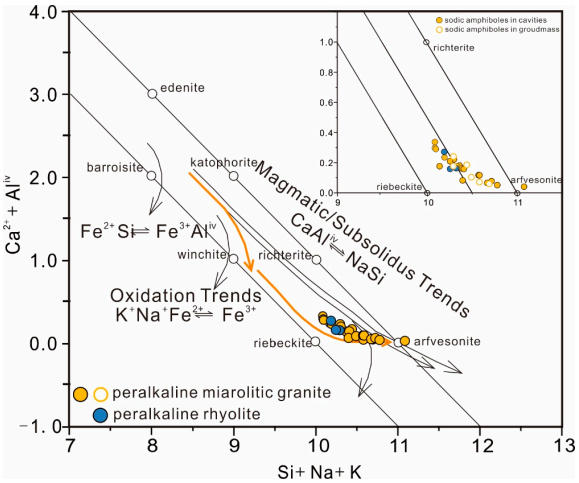

Figure 9. Cationic Si + Na + K versus Ca^{2+} + Al^{IV} plots (apfu) for sodic amphibole from the peralkaline granitic dikes compositional trends for Serra da Graciosa Alkaline Association 2, Graciosa Province [62]; fields after Strong and Taylor [61].

5. Discussion

5.1. Genesis of the Peralkaline Granitic Rocks

The development of arfvedsonites in all of the samples and their high Zr + Nb + Ce + Y (1055~3932 ppm) contents, 10,000 × Ga/Al (3.6~6.9) ratios (Figure 10a), large-ion lithophile elements (LILE) abundances (e.g., Rb, Th, U, and K), low CaO and P_2O_5 contents, and depletion in Eu, Ba, Sr, Ti, and P indicates that the peralkaline granitic rocks are typical peralkaline A-type granite [63,64].

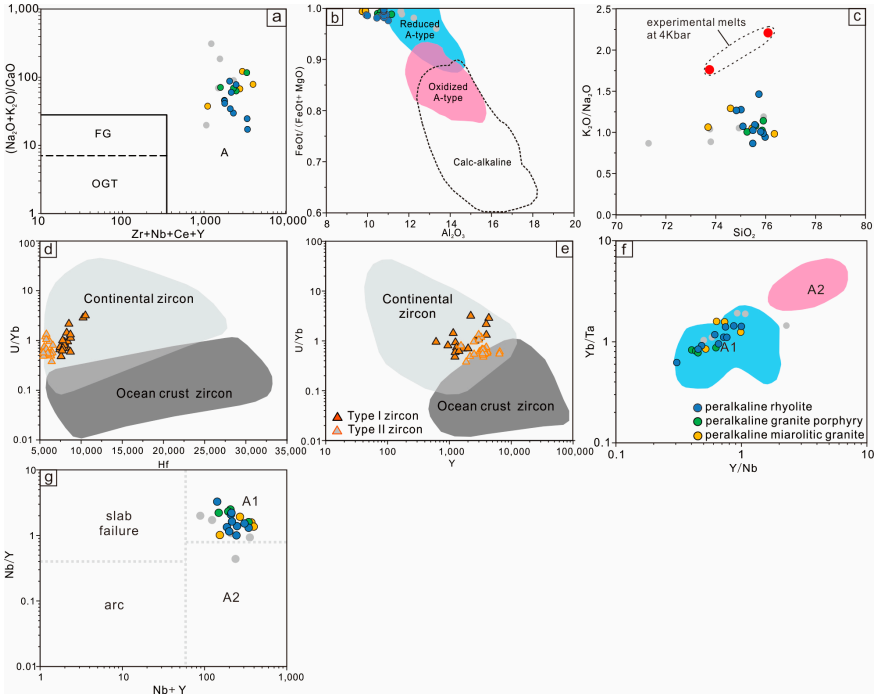

Figure 10. (**a**) $(K_2O + Na_2O)/CaO$ versus (Zr + Nb + Ce + Y) diagram of Whalen, Currie [64]; (**b**) $FeO^t/(FeO^t + MgO)$ versus Al_2O_3; fields after Dall'Agnol and de Oliveira [65]; (**c**) K_2O/Na_2O versus SiO_2; Data sources of experimental melts are from Patiño Douce [66]; (**d**) U/Yb versus Y; and (**e**) U/Yb versus Hf; fields after Grimes, John [67]; (**f**) Yb/Ta versus Y/Nb; fields after [Rehman, Khan [68], Schiller and Finger [69]]; (**g**) Nb + Y versus Nb/Y; fields after Whalen and Hildebrand [70].

A-type granite has commonly been proposed to be generated from (1) mantle-derived alkaline mafic rocks with extensive differentiation [71–74], (2) partial melting of various crustal rocks [54,64,66,75–82], and (3) a mixture of both mantle and crustal materials [83–88]. Although the whole-rock geochemical characteristics of the studied sample are close to the Ferroan Granitoids derived by the fractionation of a mafic magma (Figure 5b,c), the diagram (Figure 10b) shows that the samples in this paper belong to reductive A-type granite. In addition, if the high-silica magma derives from mantle-derived magma directly, then the high-silica magma only represents the last <5% of differentiation [11]. However, rare basic rocks occurred in the study area, indicating that the peralkaline granitic dikes were not formed by the fractional crystallization of mantle-derived magma. Because of the homogeneous Hf isotopic compositions and low calcium and magnesium contents, coupled with the lack of mingling textures in the peralkaline granitic dikes, we suggest that the peralkaline granitic dikes were formed by the partial melting of crustal materials rather than magma mixing between crust- and mantle-derived magmas.

In crust partial melting models, a diversity of crustal protoliths was proposed, including (1) residual felsic granulite after the extraction of I-type magmas [89,90]; (2) metasedimentary rocks under high temperature [75]; (3) dehydration melting of calc-alkaline rocks at low pressure [77,91]; (4) dehydrated charnockite [76,90,92]; and (5) hydrothermal-altered residual oceanic crust [35].

Residue felsic granulitic origin for A-type peralkaline granitic dikes is considered impossible because this type of magma will be enriched in Ca and A1 (in plagioclase) and Mg and Fe (in pyroxenes ± amphibole) and depleted in K and Si relative to the original protolith, which contrasts with the observed peralkaline granitic samples (high SiO_2 and $Na_2O + K_2O$ content, low CaO and MgO content as mentioned above). Moreover, the samples in this study have relatively high (K + Na)/Ca and Fe/Mg ratios, which is also opposite to the geochemical characteristics of rocks formed by the partial melting of residue felsic granulite [54,66,93]. The high positive $\varepsilon_{Hf}(t)$ values in this study also preclude the origin of metasedimentary rocks [75]. Patiño Douce [66] proposed that dehydration melting of calc-alkaline rocks (hornblende- and biotite-bearing granitoids) under low pressure ($P \leq 4$ kbar, depth ≤ 15 km) are consistent with the geochemical characteristics of A-type granitic rocks. However, the numerical simulation results show that the underplating basaltic magma cannot provide sufficient heat for the remelting of crustal material at depths less than 17 km [94,95]. Moreover, the studied samples have a high Fe-index (Figure 5c) and lower K_2O/Na_2O ratios (Figure 10c), which is distinct from the experiment results proposed by Patiño Douce [66].

The $\delta^{18}O$ values of magmatic zircons from 801 barren granites range from +2.79‰ to +5.10‰, slightly lower than the mantle zircon ($\delta^{18}O = 5.3‰ \pm 0.3‰$), which was considered to be related to the partial melting of the oceanic crust that underwent high-temperature seawater hydrothermal alteration [27,35]. In the late Early Cretaceous, the extensional tectonic setting of the Great Xingan Range is generally recognized [82,96,97], and the source of the partially melted oceanic crust is unknown. The discrimination diagrams of the zircon genetic type (Figure 10e,f) show a continental crust origin. Some studies suggested that the change in oxygen isotope composition during the evolution from a magmatic system to a hydrothermal system may follow the mechanism of isotope fractionation [98,99], and the reduction of oxygen isotope of magmatic zircon may be caused by following the Rayleigh fractionation. According to previous studies, the whole rock REE distribution of Baerzhe granite shows the tetrad effect of REE, which is most visible in late magmatic differentiates with strong hydrothermal interactions or deuteric alteration [20]. Hydrothermal zircons, which are obviously different from magmatic zircons in morphology and trace element characteristics, are believed to be crystallized in hydrothermal fluids [21], and many economic minerals are also believed to be precipitated in the hydrothermal stage [22], indicating that the Baerzhe granite has suffered the hydrothermal stage. Therefore, we believe that the partial melting of altered oceanic crust is not a possible magma source.

A-type granites derived from dehydrated charnockite lower crust usually show positive zircon $\varepsilon_{Hf}(t)$ values, which are generally related to the remelting of juvenile crustal rocks in an arc-related environment [100]. The Hf isotopic data of all the peralkaline granitic samples are plotted between the depleted mantle and chondrites (Figure 7a); two-stage Hf model ages (T_{DM2}) are mainly concentrated between 700 and 800 Ma (Figure 7b), indicating that the partial melting of dehydrated charnockite may be the magma source for rocks in this study. The negative anomalies of Ba, Sr, and Eu of the A-type peralkaline granitic dikes in this study indicate that there are plagioclase residues in the magma source or that the original magma has undergone plagioclase fractionation, which can preferably extract Al over Na in the magma, and lead to the production of peralkaline granitic magma [93]. In addition, the fluorine will increase the incompatibility of Na in the magma, which also causes the magma to evolve toward peralkaline affinity [101]. The high F contents of sodic amphiboles in the cavities of the peralkaline miarolitic granite indicate that the magma contains F-rich volatiles, which promotes the evolution of peralkaline magma.

Above all, we propose that parental magma of the peralkaline granitic dikes may be formed by the partial melting of dehydrated charnockite, and the fractionation of feldspar and the enrichment of F-rich volatiles jointly promoted the evolution of the residual melts to peralkaline magma.

5.2. Possible Relationship between Baerzhe Granites and Peralkaline Granitic Dikes: Magma Evolution

A possible genetic connection between the Baerzhe granites and the peralkaline granitic dikes in this study has been suggested because of their close temporal and spatial association, similar mineral assemblages, and geochemical features. Temporally, the peralkaline granitic dikes have consistent U-Pb ages with the Baerzhe granites; spatially, the peralkaline granitic dikes and Baerzhe mineralized granites commonly occur together, forming a subvolcanic–plutonic association. Both in the peralkaline granite porphyry and peralkaline rhyolite, we found that glomeroporphyritic texture is developed (Figures 2b and 3c). The glomeroporphyritic aggregates are coarse-grained K-feldspar, quartz, and sodic-amphiboles, which are similar to the Baerzhe barren granite. Such glomeroporphyritic aggregates are generally considered to be related to the physical accumulation of minerals [102], indicating that the Baerzhe barren granites might be residual mineral aggregates. The diagrams of $TFe_2O_3/\delta Eu$ versus Al_2O_3 (Figure 5f,g) show a consistent evolution trend from Baerzhe barren granite to peralkaline dikes.

For better constraint of the magma evolution between the Baerzhe barren granites and the peralkaline granitic dikes in the study area, we use FC–AFC–FCA and a mixing modeler [103] to simulate the magma evolution (results in Figure 11). In an alkali system, the solubility of Zr is really high (up to 7250 ppm at molar $[(Na_2O + K_2O)/Al_2O_3] = 1.18$) and positively correlated with NK/A ($(Na_2O + K_2O)/Al_2O_3$ molar) [104], so Zr can be highly enriched in alkali magma [105]. The NK/A ratios of most of the studied samples are >1, indicating that they crystallized from a peralkaline magma system. According to the geochemical profiles of the arfvedsonite in peralkaline miarolitic granite, the magma is gradually rich in F and alkali with ongoing of differentiation. In the Si + Na + K versus $Ca^{2+} + Al^{iv}$ diagram (Figure 9), the amphibole geochemical variations partially overlap the evolved trend that was found in the Serra da Graciosa Alkaline Association 2, Graciosa Province, where crystallization took place under reducing conditions with high alkalinity [62], also indicating a peralkaline magma system. In addition, the fractionation of zircon will lead to a decrease in the Zr/Hf ratios [106], while the Zr/Hf ratios of the samples in this paper are relatively uniform (30–40, Figure 11a), indicating that there was no zircon fractionation. Therefore, zirconium can be the indicator of the evolution of magma. During fractionation, Zr is gradually enriched in the residual melts. The used mineral/melt partition coefficients of trace elements are listed in Supplementary Table S6. Sample B2–8 with the lowest Zr content was chosen to represent the parent melt. According to the mineral composition of the Baerzhe barren granite, we assumed the fractionated minerals were composed of 30% amphiboles and 60% K-feldspar, with minor plagioclase

(7%), magnetite (2%), and Ilmenite (1%) (due to the low contents of trace elements in quartz, we did not evaluate the fractionation of quartz). Our model shows that the wide range of Nb and Ta contents and K/Rb ratios of the peralkaline granitic rocks from the Baerzhe area can be generated by the parental melt (B2–8) after 55%–85% fractionation. These model results confirm a magmatic connection between the Baerzhe barren granites and the peralkaline granitic dikes. The peralkaline granitic dikes can be generated by Baerzhe barren granitic magma after the extreme fractionation of K-feldspar and amphiboles.

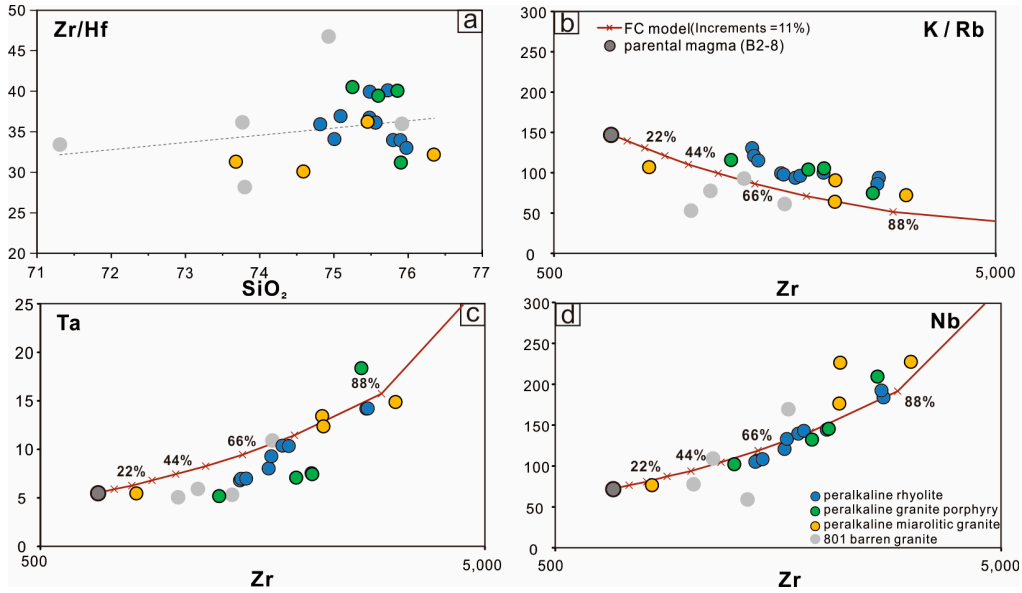

Figure 11. Diagrams of Zr/Hf versus SiO_2 and K/Rb-/Ta-/Nb versus Zr for the peralkaline granitic dikes. Rayleigh fractionation crystallization (FC) modeling results in terms of Zr versus K/Rb ratios/Ta/Nb for the peralkaline granitic dikes. The brown curved arrows in diagrams represent the predicted chemical evolution of the parental magma (B2–8) of the peralkaline granitic dikes. (**a**) Zr/Hf versus SiO_2; (**b**) K/Rb versus SiO_2; (**c**) Ta versus SiO_2; (**d**) Nb versus SiO_2.

Zircon trace elements can be used to reveal crystallization conditions and magmatic processes [58,59]. For example, the zircon Sm/Gd value changes little with fractional crystallization because of similar zircon-melt partition coefficients, reflecting the evolving melt Sm/Gd value [59]; the positive correlation between zircon Th/U and T likely reflects the combined effect of the temperature and co-crystallization of monazite [58]. The existence of the two types of zircons indicated that they were crystallized in different magma conditions. The Sm/Gd versus Y and Th/U versus T diagrams (Figure 7h,i) show that the Type II zircons crystallized in more evolved melts. The Eu anomalies of zircon are controlled by the redox state of the magma and the fractional crystallization of feldspar [107,108]. The lack of a positive correlation between the Eu/Eu* and Ce/Ce* anomalies for the studied zircons suggests that fractionation was the main dominant factor for Eu anomalies. In the Zr/Hf versus Eu/Eu* diagram (Figure 7g), the Eu/Eu* values of Type I and II zircon are higher and lower than that of the whole rock, respectively. The lower Eu/Eu* values can be explained by the crystallization of zircon after/together with plagioclase, whereas higher values suggest that zircon crystallized before the plagioclase fractionation [109]. Moreover, there is an obvious gap between these two types of zircons, which is inconsistent with a continuous magma evolution. Based on the above discussion, we suggest that these two types of zircons were crystallized in different magmatic environments: the Type II zircons were crystallized in the more evolved melt and were rapidly crystallized during magma eruption. This is also supported by their undeveloped zoning. Type I zircon is the product of intergrowth with accumulated crystals in the magma chamber.

The Type II zircons mainly occurred in the peralkaline rhyolites; these zircons have a low Ti content (Figure 7e), indicating that they crystalized in cold conditions during the late stage of magma evolution, which is consistent with the interstitial structure we observed (Figure 4b). The incompatible elements gradually enriched in the residual and more evolved melt, which may also be the reason for the relatively high LREE content of Type II zircons. The peralkaline rhyolites, which have few phenocrysts, may have been formed by the residual melt. Compared with type II zircons, type I zircons have a relatively lower evolution degree and mainly exist in peralkaline granite porphyry, which contained more phenocrysts. Type I zircons and phenocrysts may represent accumulated crystals captured from magma chambers during magma eruption.

When considering the petrographic evidence, whole-rock geochemical characteristics, and zircon trace elements, we suggest that the magma for the Baerzhe barren granites represents the residual mineral phases, and the peralkaline granitic dikes are formed by the eruption of interstitial melts concentrating in the upper magma chamber (Figure 12). The peralkaline granite porphyry may contain more cumulate minerals, and the peralkaline rhyolites consist of more melt components. The peralkaline miarolitic granite may be formed by the melt with more advanced evolution, which is evidenced by the youngest weighted mean $^{206}Pb/^{238}U$ age. From Baerzhe barren granite, peralkaline granite porphyry, and peralkaline rhyolite to peralkaline miarolitic granite, the incompatible elements (such as REE, Zr, Nb, and Ta) gradually enriched in the residual melts, accompanied by the enrichment of volatiles. The development of sodium alteration in the peralkaline miarolitic granite may have been caused by metasomatism of immiscible F-rich melt during the late stage of magma evolution [110].

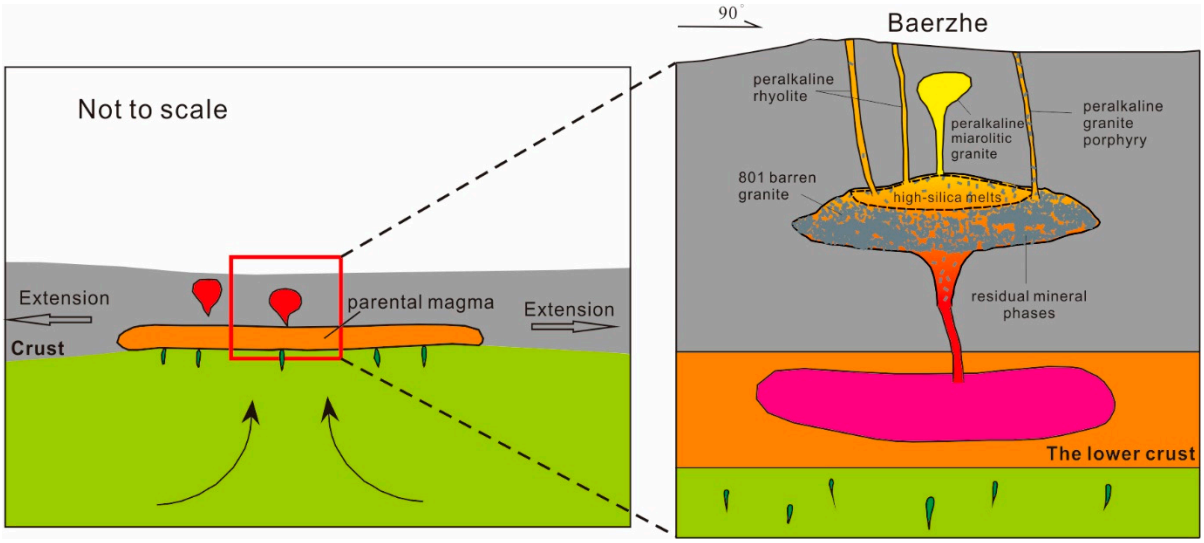

Figure 12. Cartoon illustrating the temporal evolution of plutonic–subvolcanic connections for peralkaline granitic dikes and Baerzhe granites. See the text for a detailed explanation of the models.

A-type granites typically represent an extensional tectonic setting [64,96]. Early Cretaceous A-type granites in the Great Xingan Range were emplaced within NNE–NE extensional faults, implying an extensional environment in the area at this time [111–114]. In the Yb/Ta versus Y/Nb and Nb/Y versus (Nb + Y) diagrams (Figure 10f,g), all samples are plotted in the A1 type rock area, which also supports that the rocks were within an intraplate extensional setting. In the extensional tectonic setting of the late Early Cretaceous, the involvement of the upwelling mantle magma not only induced the melting of the lower crust to form the peralkaline granitic dikes with A-type affinities, but the continuous input of heat also reactivated or prolonged the evolutionary process of the previously formed crystal mush chamber that was either solidified or partially solidified, so that it can highly evolve and form the peralkaline A-type granitic dikes at Baerzhe.

6. Conclusions

(1) The newly discovered peralkaline granitic dikes in the Baerzhe area were formed during the late Early Cretaceous (121–125 Ma), with peralkaline A-type affinities. These peralkaline granitic dikes were formed by the partial melting of dehydrated charnockite in the young lower crust with plagioclase-dominated crystal fractionation.

(2) The peralkaline granitic dikes and coeval Baerzhe plutons were formed in a uniform magma chamber. The simulation results show that the peralkaline granitic dikes can be generated by the Baerzhe barren granitic magma after extreme crystal fractionation of K-feldspar and sodic amphiboles.

(3) We suggest that the Baerzhe barren granite is from the residual mineral phases, and the peralkaline granitic dikes represent more evolved melts in the upper magma chamber.

Supplementary Materials: The following are available online at https://www.mdpi.com/article/10.3390/min12121532/s1, Table S1: Whole-rock major and trace element data of the peralkaline granitic dikes and 801 barren granites from Baerzhe area, Inner Mongolia; Table S2: LA-ICP-MS zircon data of the study samples; Table S3: Zircon Hf isotopic composition of the study samples; Table S4: Zircon trace elements of the study samples; Table S5: Compositions and formulae of the amphibole group minerals of the peralkaline granitic dikes; Table S6: Used partition coefficients of elements between mineral and melt in FC-AFC-FAC-Mixing modeling.

Author Contributions: Conceptualization, L.T. and J.G.; Field investigation, D.S., J.G., L.T. and Z.F.; Experimental analysis, L.T., D.Z. and Y.H.; Software, L.T.; Resources, D.S. and S.J.; Data Curation, L.T.; Writing—Original Draft Preparation, L.T.; Writing—Review and Editing, L.T., J.G. and D.S.; Visualization, J.G. and Z.F.; Funding Acquisition, D.S. and J.G. All authors have read and agreed to the published version of the manuscript.

Funding: This work was supported by the China National Uranium Co., Ltd., and the No. 243 Team of China Nuclear Industry (Grant No. 202003), the State Key Laboratory of Ore Deposit Geochemistry open project foundation (Grant No. 201903), Fundamental Science on Radioactive Geology and Exploration Technology Laboratory, East China University of Technology (Grant No. 2020RGET02), and the Graduate Innovation Fund of Jilin University (101832020CX214).

Data Availability Statement: The data presented in this study are available in the Supplementary Materials.

Acknowledgments: We appreciate the assistance of Ting-ting Xiao with the whole-rock major and trace elements analysis and Xiang Li with mineral composition analysis.

Conflicts of Interest: The authors declare no conflict of interest.

References

1. Annen, C. From plutons to magma chambers: Thermal constraints on the accumulation of eruptible silicic magma in the upper crust. *Earth Planet. Sci. Lett.* **2009**, *284*, 409–416. [CrossRef]
2. Annen, C.; Blundy, J.D.; Leuthold, J.; Sparks, R.S.J. Construction and evolution of igneous bodies: Towards an integrated perspective of crustal magmatism. *Lithos* **2015**, *230*, 206–221. [CrossRef]
3. Glazner, A.F.; Coleman, D.S.; Mills, R.D. *The Volcanic-Plutonic Connection*; Springer: Berlin/Heidelberg, Germany, 2015; pp. 61–82. [CrossRef]
4. Bachmann, O. On the Origin of Crystal-poor Rhyolites: Extracted from Batholithic Crystal Mushes. *J. Petrol.* **2004**, *45*, 1565–1582. [CrossRef]
5. Bachmann, O.; Bergantz, G.W. Rhyolites and their Source Mushes across Tectonic Settings. *J. Petrol.* **2008**, *49*, 2277–2285. [CrossRef]
6. Glazner, A.F.; Bartley, J.M.; Coleman, D.S.; Gray, W.; Taylor, R.Z. Are plutons assembled over millions of years by amalgamation from small magma chambers? *GSA Today* **2004**, *14*, 4–12. [CrossRef]
7. Zhang, J.-H.; Yang, J.-H.; Chen, J.-Y.; Wu, F.-Y.; Wilde, S.A. Genesis of late Early Cretaceous high-silica rhyolites in eastern Zhejiang Province, southeast China: A crystal mush origin with mantle input. *Lithos* **2018**, *296–299*, 482–495. [CrossRef]
8. Yan, L.-L.; He, Z.-Y.; Beier, C.; Klemd, R. Zircon trace element constrains on the link between volcanism and plutonism in SE China. *Lithos* **2018**, *320–321*, 28–34. [CrossRef]
9. Chen, S.-R.; Wang, Q.; Zhu, D.-C.; Weinberg, R.F.; Zhang, L.-L.; Zhao, Z.-D. Reheating and Magma Mixing Recorded by Zircon and Quartz from High-Silica Rhyolite in the Coqen Region, Southern Tibet. *Am. Mineral.* **2021**, *106*, 112–122. [CrossRef]

10. Bachmann, O.; Miller, C.F.; de Silva, S.L. The volcanic–plutonic connection as a stage for understanding crustal magmatism. *J. Volcanol. Geotherm. Res.* **2007**, *167*, 1–23. [CrossRef]
11. Lee, C.-T.A.; Morton, D.M. High silica granites: Terminal porosity and crystal settling in shallow magma chambers. *Earth Planet. Sci. Lett.* **2015**, *409*, 23–31. [CrossRef]
12. Feng, Z.; Sun, D.-Y.; Gou, J. Differentiation of magma composition: Reactivation of mush and melt reaction in a magma chamber. *Lithos* **2021**, *388–389*, 106066. [CrossRef]
13. Bachmann, O.; Bergantz, G.W. Deciphering Magma Chamber Dynamics from Styles of Compositional Zoning in Large Silicic Ash Flow Sheets. *Rev. Mineral. Geochem.* **2008**, *69*, 651–674. [CrossRef]
14. Wolff, J.A.; Ellis, B.S.; Ramos, F.C.; Starkel, W.A.; Boroughs, S.; Olin, P.H.; Bachmann, O. Remelting of cumulates as a process for producing chemical zoning in silicic tuffs: A comparison of cool, wet and hot, dry rhyolitic magma systems. *Lithos* **2015**, *236–237*, 275–286. [CrossRef]
15. Sparks, R.S.J.; Annen, C.; Blundy, J.D.; Cashman, K.V.; Rust, A.C.; Jackson, M.D. Formation and dynamics of magma reservoirs. *Philos. Trans. R. Soc. A Math. Phys. Eng. Sci.* **2019**, *377*, 20180019. [CrossRef]
16. Cooper, K.M.; Kent, A.J. Rapid remobilization of magmatic crystals kept in cold storage. *Nature* **2014**, *506*, 480–483. [CrossRef]
17. Gelman, S.E.; Deering, C.D.; Bachmann, O.; Huber, C.; Gutiérrez, F.J. Identifying the crystal graveyards remaining after large silicic eruptions. *Earth Planet. Sci. Lett.* **2014**, *403*, 299–306. [CrossRef]
18. Savko, K.A.; Samsonov, A.V.; Kholina, N.V.; Larionov, A.N.; Zaitseva, M.V.; Korish, E.H.; Bazikov, N.S.; Terentiev, R.A. 2.6 Ga high-Si rhyolites and granites in the Kursk Domain, Eastern Sarmatia: Petrology and application for the Archaean palaeocontinental correlations. *Precambrian Res.* **2019**, *322*, 170–192. [CrossRef]
19. Cheng, Y.; Spandler, C.; Chang, Z.; Clarke, G. Volcanic–plutonic connections and metal fertility of highly evolved magma systems: A case study from the Herberton Sn–W–Mo Mineral Field, Queensland, Australia. *Earth Planet. Sci. Lett.* **2018**, *486*, 84–93. [CrossRef]
20. Jahn, B.M.; Wu, F.; Capdevila, R.; Martineau, F.; Zhao, Z.; Wang, Y. Highly evolved juvenile granites with tetrad REE patterns: The Woduhe and Baerzhe granites from the Great Xing'an Mountains in NE China. *Lithos* **2001**, *59*, 171–198. [CrossRef]
21. Yang, W.-B.; Niu, H.-C.; Li, N.-B.; Hollings, P.; Zurevinski, S.; Xing, C.-M. Enrichment of REE and HFSE during the magmatic-hydrothermal evolution of the Baerzhe alkaline granite, NE China: Implications for rare metal mineralization. *Lithos* **2020**, *358–359*, 105411. [CrossRef]
22. Wu, M.; Samson, I.M.; Qiu, K.; Zhang, D. Concentration Mechanisms of Rare Earth Element-Nb-Zr-Be Mineralization in the Baerzhe Deposit, Northeast China: Insights from Textural and Chemical Features of Amphibole and Rare Metal Minerals. *Econ. Geol.* **2021**, *116*, 651–679. [CrossRef]
23. Zhao, Z.; Xiong, X.; Han, X.; Wang, Y.; Wang, Q.; Bao, Z.; Borming, J. Controls on the REE tetrad effect in granites: Evidence from the Qianlishan and Baerzhe Granites, China. *Geochem. J.* **2002**, *36*, 527–543. [CrossRef]
24. Su, H.-M.; Jiang, S.-Y.; Zhu, X.-Y.; Duan, Z.-P.; Huang, X.-K.; Zou, T. Magmatic-hydrothermal processes and controls on rare-metal enrichment of the Baerzhe peralkaline granitic pluton, inner Mongolia, northeastern China. *Ore Geol. Rev.* **2021**, *131*, 103984. [CrossRef]
25. Wubin, Y.; Hecai, N.; Qiang, S.; Yong, L.; Xueyuan, Y.; Yuzhuo, Q. Ore-forming mechanism of the Baerzhe super-large rare and rare earth elements deposit. *Acta Petrol. Sin.* **2009**, *25*, 2924–2932.
26. Yang, W.-B.; Shan, Q.; Zhao, Z.; Luo, Y.; Yu, X.; Li, N.-B.; Niu, H. Petrogenic and Metallogenic Action of the Alkaline Granitoids in Baerzhe Area: A Comparison Between Mineralized and Barren Plutons. *J. Jilin Univ. Earth Sci. Ed.* **2011**, *41*, 1689–1704.
27. Yang, W.-B.; Niu, H.-C.; Shan, Q.; Sun, W.-D.; Zhang, H.; Li, N.-B.; Jiang, Y.-H.; Yu, X.-Y. Geochemistry of magmatic and hydrothermal zircon from the highly evolved Baerzhe alkaline granite: Implications for Zr–REE–Nb mineralization. *Miner. Depos.* **2013**, *49*, 451–470. [CrossRef]
28. Wei, C.S.; Zheng, Y.F.; Zhao, Z.F.; Valley, J.W. Oxygen and neodymium isotope evidence for recycling of juvenile crust in northeast China. *Geology* **2002**, *30*, 375–378. [CrossRef]
29. Wu, F.Y.; Ye, M.; Zhang, S.H. The geodynamic model of the Manzhouli-Suifenhe geoscience transect. *J. Earth Sci.* **1995**, *20*, 535–539.
30. Jahn, B.-M.; Capdevila, R.; Liu, D.; Vernon, A.; Badarch, G. Sources of Phanerozoic granitoids in the transect Bayanhongor–Ulaan Baatar, Mongolia: Geochemical and Nd isotopic evidence, and implications for Phanerozoic crustal growth. *J. Asian Earth Sci.* **2004**, *23*, 629–653. [CrossRef]
31. Li, J.Y. Permian geodynamic setting of Northeast China and adjacent regions: Closure of the Paleo-Asian Ocean and subduction of the Paleo-Pacific Plate. *J. Asian Earth Sci.* **2006**, *26*, 207–224. [CrossRef]
32. Zhou, J.-B.; Wilde, S.A. The crustal accretion history and tectonic evolution of the NE China segment of the Central Asian Orogenic Belt. *Gondwana Res.* **2013**, *23*, 1365–1377. [CrossRef]
33. Wu, F.-Y.; Sun, D.-Y.; Ge, W.-C.; Zhang, Y.-B.; Grant, M.L.; Wilde, S.A.; Jahn, B.-M. Geochronology of the Phanerozoic granitoids in northeastern China. *J. Asian Earth Sci.* **2011**, *41*, 1–30. [CrossRef]
34. Deng, C.; Gou, J.; Sun, D.; Sun, G.; Tian, Z.; Lehmann, B.; Moynier, F.; Yin, R. Mercury isotopic composition of igneous rocks from an accretionary orogen: Implications for lithospheric recycling. *Geology* **2022**, *50*, 1001–1006. [CrossRef]
35. Zhang, J.H.; Shan, G.; Ge, W.C.; Wu, F.Y.; Ming, L. Geochronology of the Mesozoic volcanic rocks in the Great Xing'an Range, northeastern China: Implications for subduction-induced delamination. *Chem. Geol.* **2011**, *276*, 144–165. [CrossRef]

36. Tang, Z.-Y.; Sun, D.-Y.; Mao, A.-Q.; Yang, D.-G.; Deng, C.-Z. Timing and evolution of Mesozoic volcanism in the central Great Xing'an Range, northeastern China. *Geol. J.* **2019**, *54*, 3737–3754. [CrossRef]
37. Zhu, J.Z.; Zhang, G.H.; Du, Q.S.; He, J. Ore potentiality, mineralizationlaws and genesis of alkaline granite in 801 rare REE deposit. *Northwest. Geol.* **2013**, *46*, 207–214.
38. Peng, L.; Dehui, Z.; Mingqian, W.; Jilin, Z. Discussion on magma-hydrothermal formation andmineralization of granites. *Geol. Rev.* **2020**, *66*, 699–719. [CrossRef]
39. Qiu, K.; Yu, H.; Wu, M.; Geng, J.; Ge, X.; Gou, Z.; Taylor, R.D. Discrete Zr and REE mineralization of the Baerzhe rare-metal deposit, China. *Am. Mineral.* **2019**, *104*, 1487–1502. [CrossRef]
40. Qian, Y.; Sun, J.; Li, Y.; Yu, N.; Liu, J.; Li, B.; Sun, F. Geochronology, geochemistry and metallogenic dynamics of gold-polymetallic deposits in Xicha region, the northeastern margin of the North-China Platform. *Acta Petrol. Sin.* **2020**, *36*, 1127–1150. [CrossRef]
41. Liu, Y.; Zong, K.; Kelemen, P.B.; Gao, S. Geochemistry and magmatic history of eclogites and ultramafic rocks from the Chinese continental scientific drill hole: Subduction and ultrahigh-pressure metamorphism of lower crustal cumulates. *Chem. Geol.* **2008**, *247*, 133–153. [CrossRef]
42. Liu, X.; Gao, S.; Diwu, C.; Yuan, H.; Hu, Z. Simultaneous in-situ determination of U-Pb age and trace elements in zircon by LA-ICP-MS in 20 μm spot size. *Chin. Sci. Bull.* **2007**, *52*, 1257–1264. [CrossRef]
43. Wiedenbeck, M.A.P.C.; Alle, P.; Corfu, F.Y.; Griffin, W.L.; Meier, M.; Oberli, F.V.; Quadt, A.V.; Roddick, J.C.; Spiegel, W. Three natural zircon standards for U-Th-Pb, Lu-Hf, trace element and REE analyses. *Geostand. Geoanal. Res.* **1995**, *19*, 1–23. [CrossRef]
44. Sláma, J.; Košler, J.; Condon, D.J.; Crowley, J.L.; Gerdes, A.; Hanchar, J.M.; Horstwood, M.S.A.; Morris, G.A.; Nasdala, L.; Norberg, N.; et al. Plešovice zircon—A new natural reference material for U-Pb and Hf isotopic microanalysis. *Chem. Geol.* **2008**, *249*, 1–35. [CrossRef]
45. Andersen, T. Correction of common lead in U-Pb analyses that do not report 204Pb. *Chem. Geol.* **2002**, *192*, 59–79. [CrossRef]
46. Ludwig, K.R. *User's Manual for Isoplot/Ex Rev. 3.00: A Geochronological Toolkit for Microsoft Excel*; Berkeley Geochronology Center Special Publication: Berkeley, CA, USA, 2003; Volume 4.
47. Hou, K.J.; Li, Y.H.; Zou, T.R.; Qu, X.M.; Shi, Y.R.; Xie, G.Q. Laser ablation-MC-ICP-MS technique for Hf isotope microanalysis of zircon and its geological applications. *Acta Petrol. Sin.* **2007**, *23*, 2595–2604.
48. Chu, N.C.; Taylor, R.N.; Chavagnac, V.; Nesbitt, R.W.; Boella, R.M.; Milton, J.A.; German, C.R.; Bayon, G.; Burton, K. Hf isotope ratio analysis using multi-collector inductively coupled plasma mass spectrometry: An evaluation of isobaric interference corrections. *J. Anal. At. Spectrom.* **2002**, *17*, 1567–1574. [CrossRef]
49. Elhlou, S.; Belousova, E.; Griffin, W.L.; Pearson, N.J.; O'Reilly, S.Y. Trace element and isotopic composition of GJ-red zircon standard by laser ablation. *Geochim. Cosmochim. Acta* **2006**, *70*, A158. [CrossRef]
50. Hawthorne, F.C.; Oberti, R.; Harlow, G.E.; Maresch, W.V.; Martin, R.F.; Schumacher, J.C.; Welch, M.D. Nomenclature of the amphibole supergroup. *Am. Mineral.* **2012**, *97*, 2031–2048. [CrossRef]
51. Oberti, R.; Cannillo, E.; Toscani, G. How to name amphiboles after the IMA2012 report: Rules of thumb and a new PC program for monoclinic amphiboles. *Period. Mineral.* **2012**, *81*, 257–267. [CrossRef]
52. Locock, A.J. An Excel spreadsheet to classify chemical analyses of amphiboles following the IMA 2012 recommendations. *Comput. Geosci.* **2014**, *62*, 1–11. [CrossRef]
53. Shand, S. Eruptive Rocks. In *Eruptive Rocks, Their Genesis, Composition, and Classification, with a Chapter on Meteorites*; John Wiley & Sons: Hoboken, NJ, USA, 1944; pp. 101–102.
54. Frost, C.D.; Frost, B.R. On Ferroan (A-type) Granitoids: Their Compositional Variability and Modes of Origin. *J. Petrol.* **2010**, *52*, 39–53. [CrossRef]
55. Sun, W.; McDonough, W. *Chemical and Isotopic Systematics of Oceanic Basalts: Implications for Mantle Composition and Processes*; Geological Society London Special Publications: Bath, UK, 1989; Volume 42.
56. Pupin, J.P. Zircon and granite petrology. *Contrib. Mineral. Petrol.* **1980**, *73*, 207–220. [CrossRef]
57. Zhong, S.; Feng, C.; Seltmann, R.; Li, D.; Qu, H. Can magmatic zircon be distinguished from hydrothermal zircon by trace element composition? The effect of mineral inclusions on zircon trace element composition. *Lithos* **2018**, *314–315*, 646–657. [CrossRef]
58. Kirkland, C.L.; Smithies, R.H.; Taylor, R.J.M.; Evans, N.; McDonald, B. Zircon Th/U ratios in magmatic environs. *Lithos* **2015**, *212–215*, 397–414. [CrossRef]
59. Gardiner, N.J.; Hawkesworth, C.J.; Robb, L.J.; Mulder, J.A.; Wainwright, A.N.; Cawood, P.A. Metal anomalies in zircon as a record of granite-hosted mineralization. *Chem. Geol.* **2021**, *585*, 120580. [CrossRef]
60. Leake, B.E.; Woolley, A.R.; Birch, W.D.; Burke, E.A.; Ferraris, G.; Grice, J.D.; Hawthorne, F.C.; Kisch, H.J.; Krivovichev, V.G.; Schumacher, J.C.; et al. Nomenclature of amphiboles: Additions and revisions to the International Mineralogical Association's amphibole nomenclature. *Mineral. Mag.* **2018**, *68*, 209–215. [CrossRef]
61. Strong, D.; Taylor, R. Magmatic-subsolidus and oxidation trends in composition of amphiboles from silica-saturated peralkaline igneous rocks. *Mineral. Petrol.* **1984**, *32*, 211–222. [CrossRef]
62. Gualda, G.A.R.; Vlach, S.R.F. The Serra da Graciosa A-type Granites and Syenites, southern Brazil. Part 3: Magmatic evolution and post-magmatic breakdown of amphiboles of the alkaline association. *Lithos* **2007**, *93*, 328–339. [CrossRef]
63. Collins, W.J.; Beams, S.D.; White, A.J.R.; Chappell, B.W. Nature and origin of A-type granites with particular reference to southeastern Australia. *Contrib. Mineral. Petrol.* **1982**, *80*, 189–200. [CrossRef]

64. Whalen, J.B.; Currie, K.L.; Chappell, B.W. A-type granites: Geochemical characteristics, discrimination and petrogenesis. *Contrib. Mineral. Petrol.* **1987**, *95*, 407–419. [CrossRef]
65. Dall'Agnol, R.; de Oliveira, D.C. Oxidized, magnetite-series, rapakivi-type granites of Carajás, Brazil: Implications for classification and petrogenesis of A-type granites. *Lithos* **2007**, *93*, 215–233. [CrossRef]
66. Patiño Douce, A.E. Generation of metaluminous A-type granites by low-pressure melting of calc-alkaline granitoids. *Geology* **1997**, *25*, 743–746. [CrossRef]
67. Grimes, C.B.; John, B.E.; Kelemen, P.B.; Mazdab, F.K.; Wooden, J.L.; Cheadle, M.J.; Hanghøj, K.; Schwartz, J.J. Trace element chemistry of zircons from oceanic crust: A method for distinguishing detrital zircon provenance. *Geology* **2007**, *35*, 643–646. [CrossRef]
68. Rehman, H.U.; Khan, T.; Lee, H.-Y.; Chung, S.-L.; Jan, M.Q.; Zafar, T.; Murata, M. Petrogenetic source and tectonic evolution of the Neoproterozoic Nagar Parkar Igneous Complex granitoids: Evidence from zircon Hf isotope and trace element geochemistry. *Precambrian Res.* **2021**, *354*, 106047. [CrossRef]
69. Schiller, D.; Finger, F. Application of Ti-in-zircon thermometry to granite studies: Problems and possible solutions. *Contrib. Mineral. Petrol.* **2019**, *174*, 51. [CrossRef]
70. Whalen, J.B.; Hildebrand, R.S. Trace element discrimination of arc, slab failure, and A-type granitic rocks. *Lithos* **2019**, *348–349*, 105179. [CrossRef]
71. Papoutsa, A.; Pe-Piper, G.; Piper, D.J.W. Systematic mineralogical diversity in A-type granitic intrusions: Control of magmatic source and geological processes. *Bull. Geol. Soc. Am.* **2016**, *128*, 487–501. [CrossRef]
72. Turner, S.P.; Foden, J.D.; Morrison, R.S. Derivation of some A-type magmas by fractionation of basaltic magma: An example from the Padthaway Ridge, South Australia. *Lithos* **1992**, *28*, 151–179. [CrossRef]
73. Schmitt, A.K.; Emmermann, R.; Trumbull, R.B.; Bühn, B.; Henjes-Kunst, F. Petrogenesis and $^{40}Ar/^{39}Ar$ Geochronology of the Brandberg Complex, Namibia: Evidence for a Major Mantle Contribution in Metaluminous and Peralkaline Granites. *J. Petrol.* **2000**, *41*, 1207–1239. [CrossRef]
74. Liu, B.; Han, B.-F.; Ren, R.; Chen, J.-F.; Wang, Z.-Z.; Zheng, B. Petrogenesis and tectonic implications of the Early Carboniferous to the Late Permian Barleik plutons in the West Junggar (NW China). *Lithos* **2017**, *272–273*, 232–248. [CrossRef]
75. Huang, H.Q.; Li, X.H.; Li, W.X.; Li, Z.X. Formation of high δ18O fayalite-bearing A-type granite by high-temperature melting of granulitic metasedimentary rocks, southern China. *Geology* **2011**, *39*, 903–906. [CrossRef]
76. Zhao, X.-F.; Zhou, M.-F.; Li, J.-W.; Wu, F.-Y. Association of Neoproterozoic A- and I-type granites in South China: Implications for generation of A-type granites in a subduction-related environment. *Chem. Geol.* **2008**, *257*, 1–15. [CrossRef]
77. Gao, S.; Chen, W.-F.; Ling, H.-F.; Sun, L.-Q.; Ren, Q.; Xie, G.-A.; Wang, K.-X.; Tian, R.-S. A latest Jurassic A-type granite in the Middle of Inner Mongolia: Petrogenesis and tectonic implications. *Lithos* **2021**, *394–395*, 106167. [CrossRef]
78. Lv, P.; Peng, Y.; Zhang, J.; Xie, W.; Jiang, X.; Gao, X.; Ji, W.; Li, S.; Liu, Y. Paleoproterozoic multiple magmatic-metamorphic events in the Dunhuang Block, eastern Tarim Craton: Implications for assembly of the Columbia supercontinent. *Precambrian Res.* **2020**, *351*, 105949. [CrossRef]
79. Jiang, Y.; Zhao, X.; Yu, S.; Xing, G.; Yang, Z.; Shen, J.; Xu, M.; Wang, C.; Zhu, Q.; Jin, G. Geochemical and zircon U–Pb–Hf isotopic study of Early Cretaceous A-type rhyolites in Hong Kong: Implications for Palaeo-Pacific Plate subduction. *Geol. J.* **2019**, *54*, 862–878. [CrossRef]
80. Yu, S.Y.; Zhang, J.X.; Zhao, X.L.; Gong, J.H.; Li, Y.S. Geochronology, geochemistry and petrogenesis of the late Palaeoproterozoic A-type granites from the Dunhuang block, SE Tarim Craton, China: Implications for the break-up of the Columbia supercontinent. *Geol. Mag.* **2014**, *151*, 629–648. [CrossRef]
81. Gou, J.; Sun, D.Y.; Qin, Z. Late Jurassic–Early Cretaceous tectonic evolution of the Great Xing'an Range: Geochronological and geochemical evidence from granitoids and volcanic rocks in the Erguna Block, NE China. *Int. Geol. Rev.* **2019**, *61*, 1842–1863. [CrossRef]
82. Xu, G.; Deng, C.; Li, C.; Lv, C.; Yin, R.; Ding, J.; Yuan, M.; Gou, J. Petrogenesis of Late Carboniferous A-type granites and Early Cretaceous adakites of the Songnen Block, NE China: Implications for the geodynamic evolution of the Paleo-Asian and Paleo-Pacific oceans. *Lithos* **2020**, *366–367*, 105575. [CrossRef]
83. Kerr, A.; Fryer, B.J. Nd isotope evidence for crust-mantle interaction in the generation of A-type granitoid suites in Labrador, Canada. *Chem. Geol.* **1993**, *104*, 39–60. [CrossRef]
84. Yang, J.H.; Wu, F.Y.; Wilde, S.A.; Xie, L.W.; Yang, Y.H.; Liu, X.M. Tracing magma mixing in granite genesis: In situ U—Pb dating and Hf-isotope analysis of zircons. *Contrib. Mineral. Petrol.* **2007**, *153*, 177–190. [CrossRef]
85. Jiang, D.S.; Xu, X.S.; Xia, Y.; Erdmann, S. Magma Mixing in a Granite and Related Rock Association: Insight from Its Mineralogical, Petrochemical, and "Reversed Isotope" Features. *J. Geophys. Res. Solid Earth* **2018**, *123*, 2262–2285. [CrossRef]
86. Yang, J.H.; Wu, F.Y.; Wilde, S.A.; Chen, F.; Liu, X.M.; Xie, L.W. Petrogenesis of an Alkali Syenite-Granite-Rhyolite Suite in the Yanshan Fold and Thrust Belt, Eastern North China Craton: Geochronological, Geochemical and Nd-Sr-Hf Isotopic Evidence for Lithospheric Thinning. *J. Petrol.* **2007**, *49*, 315–351. [CrossRef]
87. Zhao, X.; Jiang, Y.; Yu, S.; Xing, G.; Yu, M. Geochemical, zircon U-Pb-Hf, and whole-rock Sr-Nd isotopic study of Late Jurassic Sanming A-type granite in the Wuyi area, Fujian province, Southeast China. *Geol. J.* **2017**, *53*, 2204–2218. [CrossRef]

88. Sun, X.; Ren, Y.; Sun, Z.; Wang, C.; Li, Z. Geochronology and geochemical properties of the large-scale graphite mineralization associated with the Huangyangshan alkaline pluton, Eastern Junggar, Xinjiang, NW China. *Geochemistry* **2021**, *81*, 125820. [CrossRef]
89. Liu, W.; Siebel, W.; Li, X.-J.; Pan, X.-F. Petrogenesis of the Linxi granitoids, northern Inner Mongolia of China: Constraints on basaltic underplating. *Chem. Geol.* **2005**, *219*, 5–35. [CrossRef]
90. Landenberger, B.; Collins, W.J. Derivation of A-type granites from a dehydrated charnockitic lower crust: Evidence from the Chaelundi Complex, Eastern Australia. *J. Petrol.* **1996**, *37*, 145–170. [CrossRef]
91. Patiño Douce, A.E.; Beard, J.S. Dehydration-melting of Biotite Gneiss and Quartz Amphibolite from 3 to 15 kbar. *J. Petrol.* **1995**, *36*, 707–738. [CrossRef]
92. Jiang, Y.-H.; Ling, H.-F.; Jiang, S.-Y.; Fan, H.-H.; Shen, W.-Z.; Ni, P. Petrogenesis of a Late Jurassic Peraluminous Volcanic Complex and its High-Mg, Potassic, Quenched Enclaves at Xiangshan, Southeast China. *J. Petrol.* **2005**, *46*, 1121–1154. [CrossRef]
93. Wei, C.-S.; Zhao, Z.-F.; Spicuzza, M.J. Zircon oxygen isotopic constraint on the sources of late Mesozoic A-type granites in eastern China. *Chem. Geol.* **2008**, *250*, 1–15. [CrossRef]
94. Creaser, R.; Price, R.; Wormald, R. A-type granites revisited: Assessment of a residual-source model. *Geology* **1991**, *19*, 163–166. [CrossRef]
95. Annen, C.; Sparks, R.S.J. Effects of repetitive emplacement of basaltic intrusions on thermal evolution and melt generation in the crust. *Earth Planet. Sci. Lett.* **2002**, *203*, 937–955. [CrossRef]
96. Bonin, B. A-type granites and related rocks: Evolution of a concept, problems and prospects. *Lithos* **2007**, *97*, 1–29. [CrossRef]
97. Deng, C.; Sun, D.; Han, J.; Chen, H.; Li, G.; Xiao, B.; Li, R.; Feng, Y.; Li, C.; Lu, S. Late-stage southwards subduction of the Mongol-Okhotsk oceanic slab and implications for porphyry Cu–Mo mineralization: Constraints from igneous rocks associated with the Fukeshan deposit, NE China. *Lithos* **2019**, *326*, 341–357. [CrossRef]
98. Nazari-Dehkordi, T.; Robb, L. Zircon mineral chemistry and implications for magmatic-hydrothermal evolution of the granite-hosted Zaaiplaats Sn deposit, Bushveld Large Igneous Province, South Africa. *Lithos* **2022**, *416–417*, 106672. [CrossRef]
99. Zhao, T.; Algeo, T.J.; Feng, Q.; Zi, J.-W.; Xu, G. Tracing the provenance of volcanic ash in Permian–Triassic boundary strata, South China: Constraints from inherited and syn-depositional magmatic zircons. *Palaeogeogr. Palaeoclimatol. Palaeoecol.* **2019**, *516*, 190–202. [CrossRef]
100. Ji, Z.; Meng, Q.-A.; Wan, C.-B.; Ge, W.-C.; Yang, H.; Zhang, Y.-L.; Dong, Y.; Jin, X. Early Cretaceous adakitic lavas and A-type rhyolites in the Songliao Basin, NE China: Implications for the mechanism of lithospheric extension. *Gondwana Res.* **2019**, *71*, 28–48. [CrossRef]
101. Scaillet, B.; Macdonald, R. Fluorite stability in silicic magmas. *Contrib. Mineral. Petrol.* **2004**, *147*, 319–329. [CrossRef]
102. Vernon, R.H.; Collins, W.J. Structural Criteria for Identifying Granitic Cumulates. *J. Geol.* **2011**, *119*, 127–142. [CrossRef]
103. Ersoy, Y.; Helvacı, C. FC–AFC–FCA and mixing modeler: A Microsoft® Excel© spreadsheet program for modeling geochemical differentiation of magma by crystal fractionation, crustal assimilation and mixing. *Comput. Geosci.* **2010**, *36*, 383–390. [CrossRef]
104. Watson, E.B. Zircon saturation in felsic liquids: Experimental results and applications to trace element geochemistry. *Contrib. Mineral. Petrol.* **1979**, *70*, 407–419. [CrossRef]
105. Linthout, K. Alkali-zirconosilicates in peralkaline rocks. *Contrib. Mineral. Petrol.* **1984**, *86*, 155–158. [CrossRef]
106. Lowery Claiborne, L.; Miller, C.F.; Walker, B.A.; Wooden, J.L.; Mazdab, F.K.; Bea, F. Tracking magmatic processes through Zr/Hf ratios in rocks and Hf and Ti zoning in zircons: An example from the Spirit Mountain batholith, Nevada. *Mineral. Mag.* **2018**, *70*, 517–543. [CrossRef]
107. Burnham, A.D.; Berry, A.J. An experimental study of trace element partitioning between zircon and melt as a function of oxygen fugacity. *Geochim. Cosmochim. Acta* **2012**, *95*, 196–212. [CrossRef]
108. Deng, C.; Sun, G.; Sun, D.; Han, J.; Yang, D.; Tang, Z. Morphology, trace elements, and geochronology of zircons from monzogranite in the Northeast Xing'an Block, northeastern China: Constraints on the genesis of the host magma. *Mineral. Petrol.* **2019**, *113*, 651–666. [CrossRef]
109. Słodczyk, E.; Pietranik, A.; Breitkreuz, C.; Fanning, C.M.; Anczkiewicz, R.; Ehling, B.C. Rhyolite magma evolution recorded in isotope and trace element composition of zircon from Halle Volcanic Complex. *Lithos* **2016**, *248–251*, 402–417. [CrossRef]
110. Vasyukova, O.; Williams-Jones, A.E. Fluoride–silicate melt immiscibility and its role in REE ore formation: Evidence from the Strange Lake rare metal deposit, Québec-Labrador, Canada. *Geochim. Cosmochim. Acta* **2014**, *139*, 110–130. [CrossRef]
111. Tang, Z.-Y.; Sun, D.-Y.; Mao, A.-Q. Geochemistry of Late Mesozoic volcanic rocks in the central Great Xing'an Range, NE China: Petrogenesis and crustal growth in comparison with adjacent areas. *Int. Geol. Rev.* **2019**, *62*, 1–28. [CrossRef]
112. Li, Y.; Xu, W.-L.; Tang, J.; Pei, F.-P.; Wang, F.; Sun, C.-Y. Geochronology and geochemistry of Mesozoic intrusive rocks in the Xing'an Massif of NE China: Implications for the evolution and spatial extent of the Mongol–Okhotsk tectonic regime. *Lithos* **2018**, *304–307*, 57–73. [CrossRef]
113. Deng, C.; Sun, D.; Li, G.; Lu, S.; Tang, Z.; Gou, J.; Yang, Y. Early Cretaceous volcanic rocks in the Great Xing'an Range: Late effect of a flat-slab subduction. *J. Geodyn.* **2019**, *124*, 38–51. [CrossRef]
114. Deng, C.; Sun, D.; Ping, X.; Huang, H.; Zhang, L.; Lu, S. Geochemistry of Early Cretaceous volcanic rocks in the Northeastern Great Xing'an Range, northeast China and implication for geodynamic setting. *Int. Geol. Rev.* **2019**, *61*, 1594–1612. [CrossRef]